nature metabolism

ARTICLES

https://doi.org/10.1038/s42255-022-00544-6

Check for updates

Angiocrine polyamine production regulates adiposity

Erika Monelli[1], Pilar Villacampa[1], Amaia Zabala-Letona[2,3], Anabel Martinez-Romero[1], Judith Llena[1], Daniel Beiroa[4,5], Leonor Gouveia[1,6], Iñigo Chivite[7], Sebastián Zagmutt[8], Pau Gama-Perez[9], Oscar Osorio-Conles[10,11], Laia Muixi[1], Ainara Martinez-Gonzalez[2], Sandra D. Castillo[1], Natalia Martín-Martín[2,3,12], Pau Castel[13], Lorea Valcarcel-Jimenez[2], Irene Garcia-Gonzalez[14], Josep A. Villena[11,15], Sonia Fernandez-Ruiz[2], Dolors Serra[5,8], Laura Herrero[5,8], Rui Benedito[14], Pablo Garcia-Roves[5,9], Josep Vidal[10,11], Paul Cohen[16], Rubén Nogueiras[4,5,17], Marc Claret[7,11], Arkaitz Carracedo[2,3,12,18,19,20] and Mariona Graupera[1,3,20] ✉

Reciprocal interactions between endothelial cells (ECs) and adipocytes are fundamental to maintain white adipose tissue (WAT) homeostasis, as illustrated by the activation of angiogenesis upon WAT expansion, a process that is impaired in obesity. However, the molecular mechanisms underlying the crosstalk between ECs and adipocytes remain poorly understood. Here, we show that local production of polyamines in ECs stimulates adipocyte lipolysis and regulates WAT homeostasis in mice. We promote enhanced cell-autonomous angiogenesis by deleting Pten in the murine endothelium. Endothelial Pten loss leads to a WAT-selective phenotype, characterized by reduced body weight and adiposity in pathophysiological conditions. This phenotype stems from enhanced fatty acid β-oxidation in ECs concomitant with a paracrine lipolytic action on adipocytes, accounting for reduced adiposity. Combined analysis of murine models, isolated ECs and human specimens reveals that WAT lipolysis is mediated by mTORC1-dependent production of polyamines by ECs. Our results indicate that angiocrine metabolic signals are important for WAT homeostasis and organismal metabolism.

ECs line the lumen of the entire vascular system and regulate the dynamic passage of materials and cells. They are located ubiquitously over a uniquely large surface of 4,000–7,000 m^2 covering the interface between the blood and tissues[1]. This vast contact area permits precise environmental sensing, nutrient transport and signaling integration from surrounding tissues. Therefore, ECs are regarded as the nutrient gatekeepers of the organism. Despite of this, the role of ECs in the regulation of systemic metabolism and as potential mediators of metabolic disorders remains enigmatic[2,3].

Adult ECs are largely quiescent except in some metabolic tissues where vascular expansion is considered the direct response to tissue requirements. This is the case for WAT during lipid accumulation[2] or muscle during exercise[4,5] in which adaptations to tissue function are accompanied by vascular growth. ECs mainly expand by angiogenesis, a process in which ECs sprout, branch, connect and remodel into functional vessel circuits[6,7]. Angiogenesis is guided by several extracellular cues, including growth factors, mechanical forces, flow and extracellular matrix proteins that collectively converge on intracellular growth pathways such as phosphatidylinositol 3-kinase (PI3K)/AKT/mTOR and RAS/MAPK/ERK[7,8]. Despite ECs being the first line of nutrient sensing and distribution, the role of nutrients in relation to angiogenesis and their potential impact in pathophysiology is unclear.

PTEN (phosphatase and tensin homolog) is a lipid phosphatase that dephosphorylates membrane phospholipids generated by the class I PI3Ks[9,10], the so-called phosphatidylinositol

[1]Endothelial Pathobiology and Microenviroment Group, Josep Carreras Leukaemia Research Institute (IJC), Badalona, Barcelona, Spain. [2]Center for Cooperative Research in Biosciences (CIC bioGUNE), Basque Research and Technology Alliance (BRTA), Bizkaia Technology Park, Derio, Spain. [3]Centro de Investigación Biomédica en Red de Cáncer (CIBERONC), Instituto de Salud Carlos III, Madrid, Spain. [4]CIMUS, University of Santiago de Compostela-Instituto de Investigación Sanitaria, Santiago de Compostela, Spain. [5]Centro de Investigación Biomédica en Red de Fisiopatología de la Obesidad y la Nutrición (CIBEROBN), Instituto de Salud Carlos III, Madrid, Spain. [6]Department of Immunology, Genetics and Pathology, Rudbeck Laboratory, Uppsala University, Uppsala, Sweden. [7]Neuronal Control of Metabolism Laboratory, Institut d'Investigacions Biomèdiques August Pi i Sunyer (IDIBAPS), Barcelona, Spain. [8]Department of Biochemistry and Physiology, School of Pharmacy and Food Sciences, Institut de Biomedicina de la Universitat de Barcelona (IBUB), Universitat de Barcelona, Barcelona, Spain. [9]Department of Physiological Sciences, Faculty of Medicine and Health Sciences, University of Barcelona and Bellvitge Biomedical Research Institute (IDIBELL), Barcelona, Spain. [10]Department of Endocrinology, IDIBAPS, Hospital Clinic, University of Barcelona, Barcelona, Spain. [11]Centro de Investigación Biomédica en Red de Diabetes y Enfermedades Metabólicas Asociadas (CIBERDEM), Instituto de Salud Carlos III, Madrid, Spain. [12]Traslational prostate cancer Research lab, CIC bioGUNE-Basurto, Biocruces Bizkaia Health Research Institute, Barakaldo, Spain. [13]Department of Biochemistry and Molecular Pharmacology, New York University Grossman School of Medicine, New York, NY, USA. [14]Molecular Genetics of Angiogenesis Group, Centro Nacional de Investigaciones Cardiovasculares (CNIC), Madrid, Spain. [15]Laboratory of Metabolism and Obesity, Vall d'Hebron-Institut de Recerca, Universitat Autònoma de Barcelona, Barcelona, Spain. [16]Laboratory of Molecular Metabolism, The Rockefeller University, New York, NY, USA. [17]Galician Agency of Investigation, Xunta de Galicia, La Coruña, Spain. [18]Biochemistry and Molecular Biology Department, University of the Basque Country (UPV/EHU), Bilbao, Spain. [19]Ikerbasque; Basque Foundation for Science, Bilbao, Spain. [20]These authors jointly supervised this work: Arkaitz Carracedo, Mariona Graupera. ✉e-mail: mgraupera@carrerasresearch.org

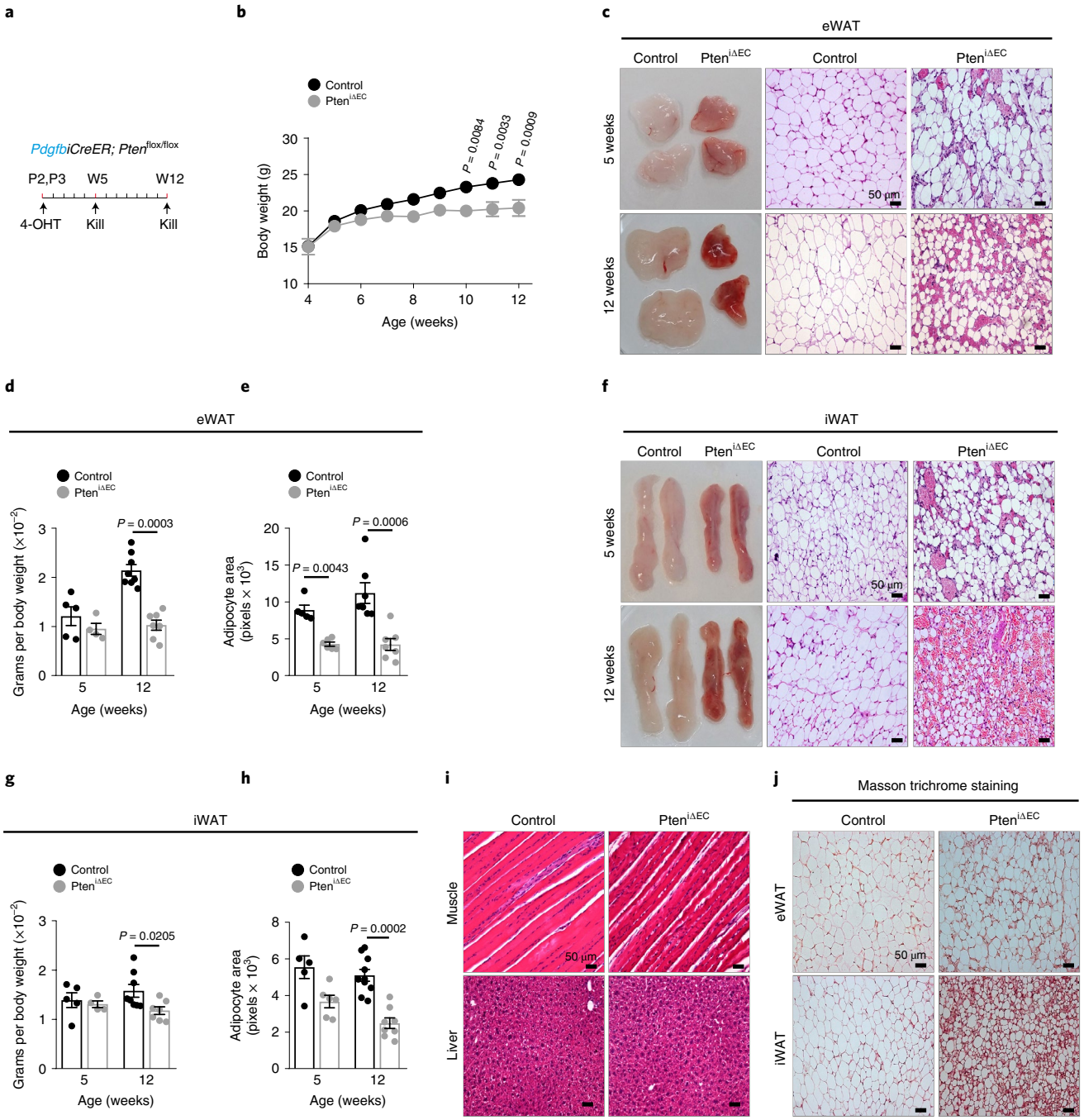

Fig. 1 | *Pten*$^{i\Delta EC}$ mice show reduced adiposity. a, Scheme illustrating the experimental protocol is shown above. **b**, Body weight curves of littermate control ($n=11$) and *Pten*$^{i\Delta EC}$ mice ($n=9$) after postnatal induction of Cre. **c**, Representative macroscopic and microscopic images of eWAT from control and *Pten*$^{i\Delta EC}$ mice at 5 and 12 weeks of age. **d**, eWAT pad weight in control and *Pten*$^{i\Delta EC}$ mice at 5 (control $n=5$; *Pten*$^{i\Delta EC}$ $n=4$) and 12 (control n = 8; *Pten*$^{i\Delta EC}$ $n=7$) weeks of age. **e**, Quantification of adipocyte area of eWAT from control and *Pten*$^{i\Delta EC}$ mice at 5 (control $n=5$; *Pten*$^{i\Delta EC}$ $n=6$) and 12 ($n=7$ each group) weeks of age. **f**, Representative macroscopic and microscopic images of iWAT from control and *Pten*$^{i\Delta EC}$ mice at 5 and 12 weeks of age. **g**, iWAT pad weight in control and *Pten*$^{i\Delta EC}$ mice at 5 (control $n=5$; *Pten*$^{i\Delta EC}$ $n=4$) and 12 (control $n=8$; *Pten*$^{i\Delta EC}$ $n=7$) weeks of age. **h**, Quantification of adipocyte area in iWAT from control and *Pten*$^{i\Delta EC}$ mice at 5 (control $n=5$;, *Pten*$^{i\Delta EC}$ $n=6$) and 12 (control $n=10$; *Pten*$^{i\Delta EC}$ $n=8$) weeks of age. **i**, Representative hematoxylin and eosin staining of muscle and liver sections from control and *Pten*$^{i\Delta EC}$ mice at 12 weeks of age. **j**, Masson trichrome fibrosis staining in eWAT and iWAT sections from control and *Pten*$^{i\Delta EC}$ mice at 12 weeks of age. Data represent mean ± s.e.m. Samples represent biological replicates. Statistical analysis was performed by the two-sided Mann–Whitney *U*-test (**d**,**e**,**g**,**h**) and two-way analysis of variance (ANOVA) with Bonferroni correction (**b**).

3,4,5-trisphosphate (PtdIns(3,4,5)P_3, also known as PIP_3). Through the generation of PIP_3, the PI3K/PTEN signaling pathway controls a plethora of cellular functions, including growth, proliferation, migration, metabolism and vesicular trafficking[8]. ECs are exquisitely sensitive to PI3K fluctuations, with both too much and too little PI3K signaling resulting in defects in vascular development[11,12]. Analysis at single-cell resolution has shown that genetic manipulation of the PI3K/PTEN pathway primarily impacts cell proliferation[11,13,14].

Here we show that ECs, through the release of specific angiokines, regulate the function of WAT with systemic metabolic implications. Forced activation of the PI3K pathway in ECs results in increased proliferation of the vessel compartment in the adipose tissue and reduced adiposity. The molecular connection between the endothelial function and adipocyte biology is underscored by a metabolite-based angiocrine communication, a process mediated by polyamines. We provide evidence showing that this unprecedented metabolic axis is relevant in pathophysiological conditions, such as obesity.

Results

Endothelial *Pten* deletion elicits a lean phenotype. To elucidate endothelium-regulated systemic metabolic processes, we developed a model of enhanced EC-autonomous angiogenesis. Given that EC proliferation is primarily governed by PI3K signaling[11,13,14], we studied the systemic consequences of sustained PI3K activity in the endothelium by *Pten* loss[14]. We bred *Pten*$^{flox/flox}$ mice[15] with *PdgfbiCreER* transgenic mice[16] (hereafter referred to as *Pten*$^{i\Delta EC}$), which enables the deletion of *Pten* in ECs in a tamoxifen-inducible manner. We administered 4-hydroxytamoxifen (4-OHT) postnatally to mice carrying conditional *Pten* knockout alleles alone or in combination with *PdgfbiCreER*. To confirm *Pten* deletion selectively in the endothelium, we took advantage of the Ribotag model[17]. This strategy allows for the analysis of actively translated messenger RNAs in a cell-specific manner in vivo, when Cre recombinase induces the expression of hemagglutinin A (HA)-tagged ribosomal protein Rpl22. We crossed these mice with *PdgfbiCreER* (hereafter referred to as *Ribotag*^{iHAEC}) and demonstrated that only the endothelium was targeted in all tissues analyzed (Extended Data Fig. 1a,b). We could confirm that the deletion of *Pten* in the endothelium occurred in all tissues studied in *Pten*$^{i\Delta EC}$-*Ribotag*^{iHAEC} mice (Extended Data Fig. 1c). Also, we validated the efficient depletion of *Pten* in isolated ECs from several tissues of *Pten*$^{i\Delta EC}$ mice (Extended Data Fig. 1d–g).

Next, we evaluated the phenotypic consequences of endothelial-specific *Pten* deletion in adult mice. Endothelial *Pten* loss was associated with a remarkable reduction in body weight and adiposity compared to control littermates, thus resulting in a lean phenotype (Fig. 1a,b). We found a selective reduction in WAT mass and adipocyte area, including both epididymal (eWAT) and inguinal (iWAT) depots (Fig. 1b–h and Extended Data Fig. 2a), a phenotype that was robust by 10 weeks of age. Nuclear magnetic resonance analysis further confirmed the reduction in overall fat mass in adult *Pten*$^{i\Delta EC}$ mice (Extended Data Fig. 2b,c). Detailed histopathological and molecular characterization did not reveal ectopic lipid deposition in muscle and liver (Fig. 1i), WAT fibrosis (Fig. 1j and Extended Data Fig. 2d,e), altered adipocyte differentiation or cell death (Extended Data Fig. 2f–j). Of note, in line with the reduction in adipose tissue mass, the circulating levels of leptin (an adipose-derived adipokine) were markedly reduced in mutant mice (Extended Data Fig. 2k).

To explore the impact of loss of endothelial *Pten* on the vasculature, we performed whole-mount or OCT-embedded section staining with isolectin B4 (IB4) or anti-CD31, two well-known markers of ECs, in several tissues. The vast majority of tissues analyzed in *Pten*$^{i\Delta EC}$ mice remained phenotypically unaffected at 12 weeks of age (Extended Data Fig. 3a,b) despite the deletion of this gene (Extended Data Fig. 1c). However, we observed vascular hyperplasia in the *Pten*$^{i\Delta EC}$ WAT, based on a progressive increase of vascular content and EC proliferation, as illustrated by enhanced IB4, ERG (EC-specific nuclear marker) and Ki67 staining (Fig. 2a–h). The vascular phenotype was already apparent by 5 weeks of age (Fig. 2a–h), a time point at which adiposity remained largely unaltered (Fig. 1d,g), indicating that vessel growth precedes the reduction in adiposity. The histological data were largely consistent with the molecular evaluation of endothelial markers using quantitative real-time PCR (Extended Data Fig. 3c). Of note, we could not observe vascular endothelial growth factor (VEGF) signaling alterations in WAT by means of *VegfA* mRNA abundance, thus suggesting no major role of this growth factor in the enhanced vascularization of *Pten*$^{i\Delta EC}$ mice (Extended Data Fig. 3d). The enhanced vascular content in *Pten*$^{i\Delta EC}$ WAT was not associated with aberrant leakiness (Extended Data Fig. 3e). Due to the regulatory and functional analogies with WAT, we performed a detailed analysis of brown adipose tissue (BAT). *Pten*$^{i\Delta EC}$ BAT showed a mild increase in the vascular content compared to control littermates (Extended Data Fig. 3a,b), although the vascular phenotype was less prominent than in WAT. In line with this, we could not observe alterations in the morphology of brown adipocytes (Extended Data Fig. 3f).

To validate the contribution of endothelial-specific *Pten* deletion on vessel density and adiposity, we carried out two complementary approaches. First, we ruled out developmental effects associated with early activation of Cre by studying the consequences of *Pten* deletion in adult mice. Administration of tamoxifen at 8 weeks of age in *Pten*$^{i\Delta EC}$ mice recapitulated the phenotype in vascularity and adiposity (Extended Data Fig. 4a–h). We also took advantage of a second inducible Cre delivery system targeted to the endothelium, under the control of the VE-Cadherin promoter[18]; the so-called *Cdh5-CreER*^{T2}. Administration of 4-OHT to *Cdh5-CreER*^{T2} postnatal mice resulted in a similar phenotype to that of the *PdgfbiCreER* model, albeit milder (Extended Data Fig. 4i–p). Together, these results reveal an adipose tissue-specific contribution of endothelial *Pten* that enables the control of adiposity.

Endothelial *Pten* loss protects from obesity. Excessive adiposity is a hallmark of obesity and is associated with suboptimal WAT vascularization[2,3,19–21]. Thus, we interrogated whether obesity-associated reduced vascularization in experimental systems and human specimens could be correlated with alterations in PTEN levels. The elevated adiposity elicited by high-fat diet (HFD) feeding in mice was associated with reduced vascularization and higher expression of *Pten* in the adipose endothelium (Extended Data Fig. 5a–c). We confirmed that reduced vascularization and elevated expression of *PTEN* is also observed in surgical specimens of visceral adipose tissue (VAT) from individuals with obesity (Extended Data Fig. 5d–f and Supplementary Table 4).

Given that induction of angiogenesis in WAT reportedly ameliorates obesity-associated metabolic complications[22–26], we predicted that our mutant mouse model would be protected from obesity. To address this, we first challenged control and *Pten*$^{i\Delta EC}$ mice with HFD. Loss of *Pten* in this context led to reduced body weight, WAT mass and adipocyte area (Fig. 3a–d), with no significant changes in other tissues (Extended Data Fig. 6a). Similar to mice fed with chow diet, *Pten*$^{i\Delta EC}$ mice showed higher vascularization in WAT upon exposure to HFD (Fig. 3e,f). Moreover, *Pten* deletion in ECs

Fig. 2 | High vascular content and enhanced EC proliferation in *Pten*$^{i\Delta EC}$ WAT. a,**c**, Representative confocal images of eWAT (**a**) and iWAT (**c**) whole-mount staining with IB4 (red) from control and *Pten*$^{i\Delta EC}$ mice at 5 (left) and 12 (right) weeks of age. **b**,**d**, Quantification of IB4-positive area in eWAT (**b**) and iWAT (**d**) from control and *Pten*$^{i\Delta EC}$ mice at 5 ($n=15$ per genotype) and 12 (control $n=8$; *Pten*$^{i\Delta EC}$ $n=6$) weeks of age. **e**,**g**, Representative images of flat-mounted eWAT (**e**) and iWAT (**g**) from 5-week-old control and *Pten*$^{i\Delta EC}$ mice stained with ERG (green), Ki67 (magenta) and IB4 (white). Yellow arrows indicate double-positive proliferating cells. **f**,**h**, Quantification of proliferating ECs (ERG and Ki67 double-positive cells) in images from flat-mounted eWAT (**f**) and iWAT (**h**) from control and 5-week-old *Pten*$^{i\Delta EC}$ mice (control $n=5$; *Pten*$^{i\Delta EC}$ $n=4$). Data represent mean ± s.e.m. Samples represent biological replicates. Statistical analysis was performed by the two-sided Mann–Whitney *U*-test (**b**,**d**,**f**,**h**).

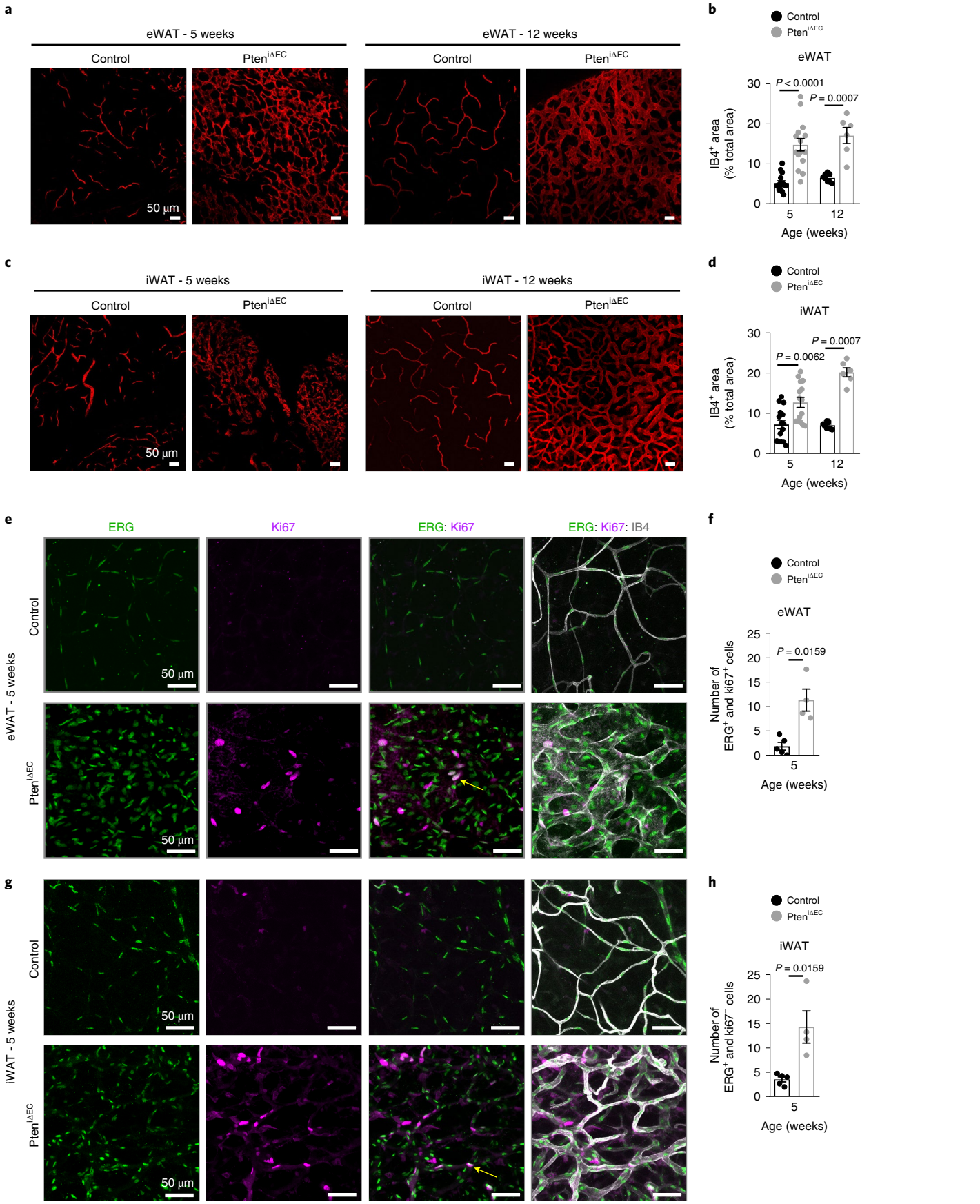
a
eWAT - 5 weeks
eWAT - 12 weeks
Control
Pten iΔEC
50 µm
b
Control
Pten iΔEC
eWAT
P < 0.0001
P = 0.0007
IB4+ area (% total area)
Age (weeks)
c
iWAT - 5 weeks
iWAT - 12 weeks
d
iWAT
P = 0.0062
P = 0.0007
e
ERG
Ki67
ERG: Ki67
ERG: Ki67: IB4
eWAT - 5 weeks
f
Number of ERG+ and ki67+ cells
P = 0.0159
g
iWAT - 5 weeks
h

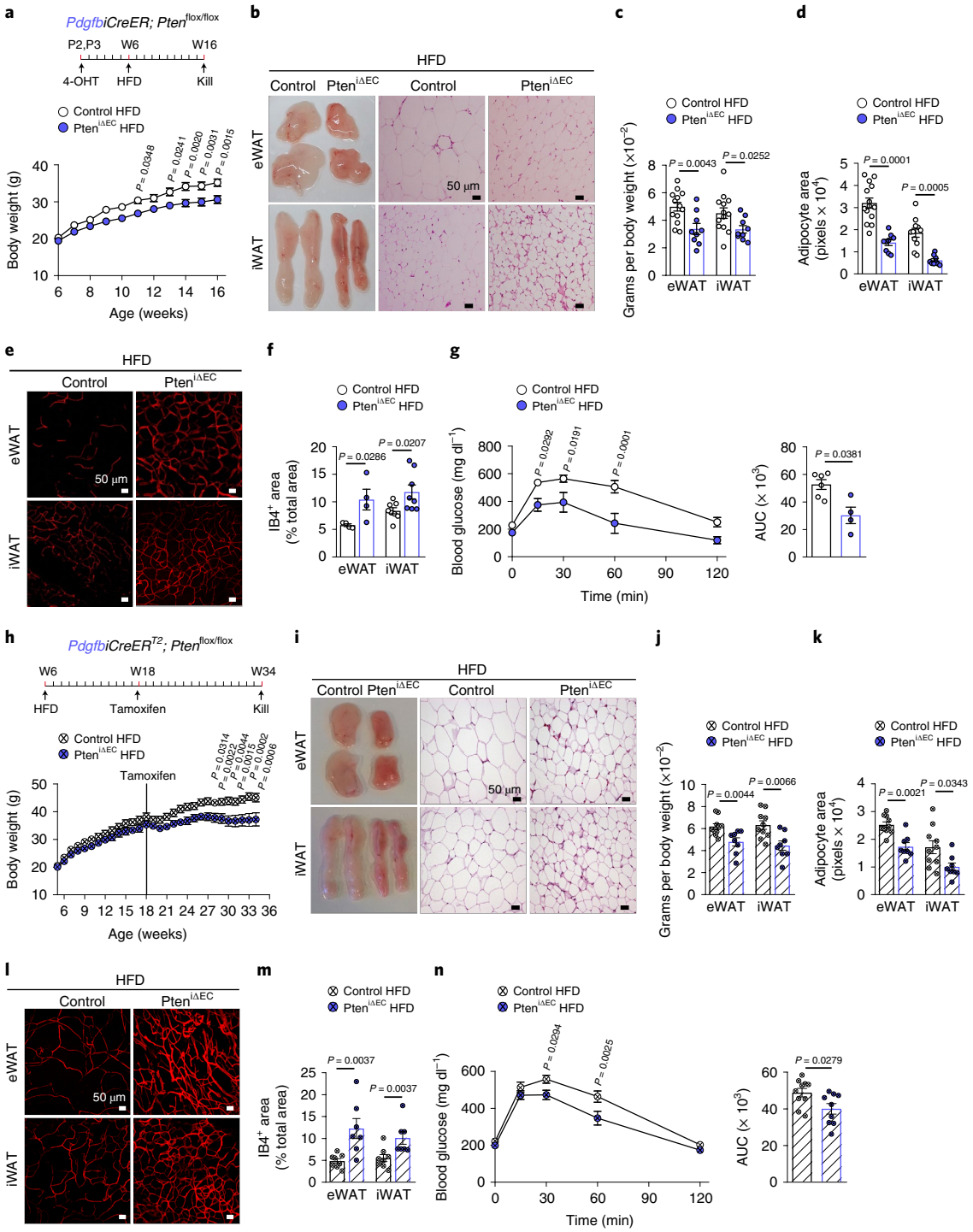

Fig. 3 | *Pten*$^{i\Delta EC}$ mice are resistant to diet-induced obesity. a, Body weight curves of control and *Pten*$^{i\Delta EC}$ mice fed with HFD for 10 weeks after postnatal induction of Cre (control $n=14$; *Pten*$^{i\Delta EC}$ $n=10$). **b**, Representative macroscopic and microscopic images of eWAT and iWAT. **c**, eWAT and iWAT pad weight (control $n=13$; *Pten*$^{i\Delta EC}$ $n=9$). **d**, Quantification of adipocyte area in eWAT (control $n=14$; *Pten*$^{i\Delta EC}$ $n=9$) and iWAT (control $n=11$; *Pten*$^{i\Delta EC}$ $n=9$). **e**, Representative images of IB4-stained blood vessels (red) in flat-mounted eWAT and iWAT. **f**, Quantification of IB4-positive area in eWAT ($n=4$ per group) and iWAT ($n=8$ per group) pad. **g**, Glucose tolerance test (GTT) performed in control and *Pten*$^{i\Delta EC}$ mice fed with HFD for 10 weeks (control $n=6$; *Pten*$^{i\Delta EC}$ $n=4$). Bars to the right show area under the curve (AUC) quantification of blood glucose monitoring during GTT (control $n=6$; *Pten*$^{i\Delta EC}$ $n=4$). **h**, Body weight curves of control and *Pten*$^{i\Delta EC}$ mice fed with HFD for 34 weeks. Cre activity was induced with tamoxifen administration at 18 weeks of age (control $n=10$; *Pten*$^{i\Delta EC}$ $n=8$). **i**, Representative macroscopic and microscopic images of eWAT and iWAT. **j**, eWAT and iWAT pad weight (control $n=10$; *Pten*$^{i\Delta EC}$ $n=9$). **k**, Quantification of adipocyte area in eWAT and iWAT (control $n=10$; *Pten*$^{i\Delta EC}$ $n=8$). **l**, Representative images of IB4-stained blood vessels (red) in flat-mounted eWAT and iWAT. **m**, Quantification of IB4-positive area in eWAT and iWAT from control and *Pten*$^{i\Delta EC}$ mice exposed to HFD for 34 weeks (control $n=8$; *Pten*$^{i\Delta EC}$ $n=7$). **n**, GTT performed in control ($n=10$) and *Pten*$^{i\Delta EC}$ ($n=9$) mice fed with HFD for 28 weeks. Bars to the right show AUC quantification of blood glucose monitoring during GTT (control $n=10$; *Pten*$^{i\Delta EC}$ $n=9$). Data represent mean ± s.e.m. Samples represent biological replicates. Statistical analysis was performed by the two-sided Mann–Whitney *U*-test (**c**,**d**,**f**,**j**,**k**,**m**) and two-way ANOVA with Bonferroni correction (**a**,**g**,**h**,**n**).

resulted in improved glucose metabolism in mice fed with HFD for 10 weeks (Fig. 3g and Extended Data Fig. 6b–d). In line with previous observations, we did not detect overt alterations in WAT fibrosis in *Pten*$^{i\Delta EC}$ mice under HFD (Extended Data Fig. 6e,f). Second, we evaluated the consequences of endothelial-specific deletion of *Pten* in established obesity (Fig. 3h). Administration of tamoxifen in mice fed with HFD for 12 weeks resulted in a robust correction of body weight, reduced adiposity, increased WAT vascularity and improved glucose tolerance in the absence of WAT fibrosis (Fig. 3h–n and Extended Data Fig. 6g–k). Together, these data indicate that endothelial PTEN is instrumental for the control of adiposity in pathophysiological conditions.

Endothelial *Pten* loss leads to enhanced WAT metabolic rate. To address how loss of *Pten* in the endothelium resulted in reduced adiposity, we monitored factors involved in nutritional uptake and energy consumption in the mouse model. Notably, the phenotype of *Pten*$^{i\Delta EC}$ mice was not due to differences in food intake, intestinal malabsorption, locomotor activity, BAT thermogenesis or Ucp1-dependent or independent WAT browning (Fig. 4a–h). However, we did detect a significant increase in energy expenditure in mutant mice, consistent with reduced adiposity (Fig. 4i). In line with this, the plasma triglyceride concentration was reduced in *Pten*$^{i\Delta EC}$ mice compared to controls (Fig. 4j). To associate the energy expenditure phenotype with the reduction in adiposity, we sought to assess metabolic activity at tissue resolution. We evaluated mitochondrial function ex vivo by high-resolution respirometry in various freshly isolated tissues. Only WAT, the tissue exhibiting the most prominent phenotype in *Pten*$^{i\Delta EC}$ mice, presented an increase in mitochondrial respiration (Fig. 4k–n). In summary, our results reveal a causal association between EC proliferation, increased local and systemic energy expenditure and reduced adiposity.

***Pten*-null EC proliferation relies on fatty acid metabolism.** The increased local energy consumption in WAT suggested that this phenotype could be due, at least in part, to enhanced metabolic activity by the mutant endothelium. Thus, we interrogated whether the unique access to lipids in the adipose tissue could favor the activation of lipid catabolic transcriptional programs in *Pten*$^{i\Delta EC}$ WAT endothelium to promote enhanced vascularization selectively in this tissue. First, we evaluated endothelial expression of genes involved in lipid catabolism in vivo (using *Pten*$^{i\Delta EC}$-*Ribotag*^{iHAEC} mice; Fig. 5a) and in isolated primary adipose ECs (Fig. 5b). Upregulated genes in *Pten*$^{i\Delta EC}$-*Ribotag*^{iHAEC} WAT endothelium included fatty acid transporters, genes involved in fatty acid β oxidation (FAO) and central regulators of cellular energy metabolic pathways. In line with our previous results, the activation of this program was unique to WAT endothelium, with no major differences in the endothelium of BAT, muscle and liver (Extended Data Fig. 7a–c). The lipid catabolic reprogramming was associated with enhanced FAO (Fig. 5c). Consistently, we observed increased mitochondrial respiration when lipids were supplemented in the medium (Fig. 5d,e), whereas no changes in glucose uptake (Extended Data Fig. 7d) or in glucose-induced oxygen consumption were observed (Fig. 5f,g). We speculated that the vascular phenotype in WAT was the result of increased local fatty acid availability. Indeed, cultured *Pten*$^{i\Delta EC}$ ECs derived from lung, a tissue that did not manifest a phenotype in vivo (Extended Data Fig. 3c), exhibited biological and metabolic features similar to adipose ECs when lipids were supplied in the medium (Extended Data Fig. 7e–i). To further investigate this, we evaluated the impact of etomoxir (a pharmacological inhibitor of FAO) on cell proliferation[27]. Etomoxir hampered the proliferative burst elicited by *Pten* loss in adipose ECs in vitro and in vivo (Fig. 5h–j) without overt macroscopic or weight alterations in any tissue analyzed (Extended Data Fig. 7j). Next, we undertook a genetic approach to selectively interfere with lipid catabolism in ECs in vivo. Our gene expression data showed a prominent increase in genes related to lipid transport, fatty acid β-oxidation and oxidative phosphorylation, which are transcriptionally regulated by PGC1 family factors (Fig. 5a,b). Also, we identified a mild upregulation of *Ppargc1b*, the transcript that encodes for Pgc1β (Fig. 5a,b). Hence, we took advantage of Pgc1β conditional knockout mice[28], which we bred into the endothelial-specific *Pten*-deficient mice. *Ppargc1b* deletion in the context of endothelial *Pten* loss partially rescued the elevation in adipose vascular density (Extended Data Fig. 7k,l). Together, these data indicate that *Pten* deletion makes ECs prone to proliferate in the presence of fatty acids, which represents a microenvironmental prerequisite for these cells.

Polyamines are prolipolytic angiocrine metabolic mediators. FAO was necessary to sustain adipose EC proliferation, whereas adiposity remained reduced both upon pharmacological and genetic blockade of fatty acid catabolism (Fig. 5k and Extended Data Fig. 7m). These data suggest that reduced adiposity is not solely the consequence of the proliferative burst of *Pten*$^{i\Delta EC}$ adipose endothelium. We hypothesized that angiocrine signals induced by *Pten* deletion were instructing a lipolytic response in adipocytes that would explain the lack of rescue in adiposity by inhibition of FAO. To explore this, we measured basal and stimulated fatty acid secretion into the media. Explants from *Pten*$^{i\Delta EC}$ WAT exhibited higher release of free fatty acids (FFAs) than control counterparts (Extended Data Fig. 8a and Fig. 6a). A similar trend was observed in primary adipocyte cultures upon exposure to conditioned medium derived from control or *Pten*$^{i\Delta EC}$ ECs (Fig. 6b). In line with this, fasted *Pten*$^{i\Delta EC}$ mice exhibited elevated circulating FFAs (Fig. 6c).

Fig. 4 | *Pten* loss in ECs correlates with enhanced lipids mobilization from WAT. a, Food intake measurement in control and *Pten*$^{i\Delta EC}$ mice at 8 and 12 weeks of age (control $n=11$; *Pten*$^{i\Delta EC}$ $n=8$). **b**, Total energy and triglyceride content in feces from 10-week-old control and *Pten*$^{i\Delta EC}$ mice ($n=7$). **c**, Locomotor activity measurements of control and *Pten*$^{i\Delta EC}$ mice at 7 weeks of age (control $n=16$; *Pten*$^{i\Delta EC}$ $n=15$). **d**, Representative images of thermographic recordings of BAT and quantification of intrascapular temperature in control and *Pten*$^{i\Delta EC}$ mice at 7 (control $n=6$; *Pten*$^{i\Delta EC}$ $n=3$) and 12 weeks of age (control $n=4$; *Pten*$^{i\Delta EC}$ $n=4$). **e**, Immunoblot analysis of Ucp1 in BAT lysates from control and *Pten*$^{i\Delta EC}$ mice. **f**, Gene expression profile of thermogenic genes in eWAT and iWAT depots from control and *Pten*$^{i\Delta EC}$ mice at 14 weeks of age (control $n=5$; *Pten*$^{i\Delta EC}$ $n=3$). **g**, Immunoblot analysis of Ucp1 in eWAT (top) and iWAT (bottom) lysates from control and *Pten*$^{i\Delta EC}$ mice. BAT control lysates were used as positive controls ($n=5$ per group). **h**, Gene expression profile of Ucp1 independent thermogenic genes in iWAT depots from control and *Pten*$^{i\Delta EC}$ mice at 14 weeks of age (control $n=5$; *Pten*$^{i\Delta EC}$ $n=6$). **i**, Energy expenditure (EE) measurement in control and *Pten*$^{i\Delta EC}$ mice of 7 weeks of age in light (day) and dark (night) conditions (control $n=16$, *Pten*$^{i\Delta EC}$ $n=15$). Graph to the left shows the average of EE at day and night per genotype. **j**, Plasma levels of triglycerides in 10-week-old control and *Pten*$^{i\Delta EC}$ mice (control $n=7$; *Pten*$^{i\Delta EC}$ $n=6$). **k**–**n**, High-resolution mitochondrial ex vivo respirometry in freshly isolated eWAT (**k**) (control $n=3$; *Pten*$^{i\Delta EC}$ $n=4$), iWAT (**l**) (control $n=5$; *Pten*$^{i\Delta EC}$ $n=6$), muscle (**m**) ($n=4$) and liver (**n**) ($n=4$) from control and *Pten*$^{i\Delta EC}$ mice at 6 weeks of age. Substrates are P, pyruvate; M, malate; G, glutamate; S, succinate. Pathways are N, NADH electron transfer pathway; S, succinate dehydrogenase-linked pathway; NS, NS-linked pathways. Respiratory rates are LEAK, leak state; OXPHOS, oxidative phosphorylation state; E, electron transfer state (ETS). Data represent mean ± s.e.m. Samples represent biological replicates. Statistical analysis was performed by one-sided *t*-test, Mann–Whitney *U*-test (**j**–**l**) and one-sided *t*-test (**i**) for hypothesis-driven analyses.

Collectively, these data demonstrate that endothelial-specific *Pten* deletion leads to elevated lipid mobilization from the adipose tissue. Stimulation of the β-adrenergic receptors (β-ADRs) activates lipolysis in WAT[29–31]. Thus, we tested the involvement of these membrane proteins in the lipolytic phenotype observed in *Pten*$^{i\Delta EC}$ mice. We treated mutant animals with the pan-β-ADR inhibitor propranolol for 4 d and then measured lipolysis in WAT explants. The results showed that propranolol reduced lipolysis in the explants, thus demonstrating that β-ADR receptor activity is relevant for endothelial *Pten* loss-induced lipolysis in WAT (Fig. 6d).

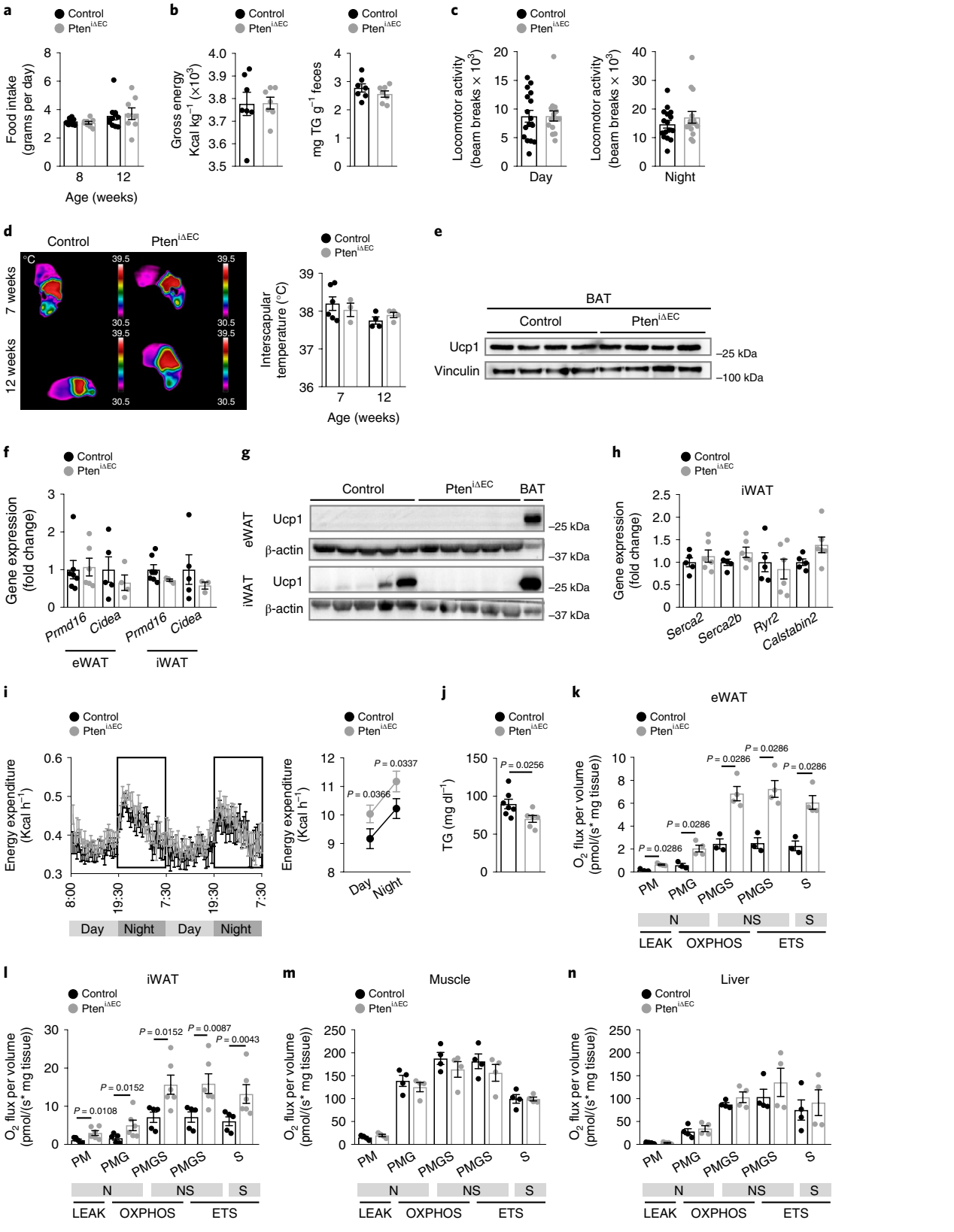

The lipolytic phenotype observed with conditioned media from *Pten*$^{i\Delta EC}$ ECs suggests that an angiocrine signal may be responsible for the metabolic effects described above. Angiocrine signals control a variety of pathophysiological processes and are emerging as key mediators of EC function and tissue homeostasis[32–34]. These molecular cues could be polypeptides, metabolites or extracellular vesicles[32–36]. To discern the identity of angiocrine signals in our model, we filtered conditioned medium to separate the metabolite fraction from that containing proteins and vesicles (Extended Data Fig. 8b). Notably, only the *Pten*$^{i\Delta EC}$ metabolite-rich conditioned medium fraction retained lipolytic activity (Fig. 6e,f). These data indicate that the angiocrine signal that stimulates lipolysis in *Pten*$^{i\Delta EC}$ WAT is a metabolite.

Next, we investigated in further detail the metabolic nature of the lipolytic angiocrine signal. To this end, we searched for metabolic pathways fulfilling three criteria: (1) to be previously linked to adiposity, (2) to exert paracrine biological effects and (3) to respond to PI3K activity. Polyamines satisfy these criteria, as they can function in a paracrine manner[37–39], reduce adiposity in the context of obesity[40–44] and it was previously reported that PI3K activation enhances polyamine synthesis to sustain oncogenicity[45,46]. Thus, we hypothesized that polyamines may act as WAT angiocrine lipolytic signals. Polyamines are polycationic metabolites synthesized from methionine and ornithine[38]. ^{13}C-methionine tracing revealed a remarkable increase in metabolites related to polyamine biosynthesis in isolated *Pten*-deficient ECs, including ^{13}C-labeled spermidine and spermine (Fig. 6g and Extended Data Fig. 8c). In line with these results, label-free metabolomics confirmed the elevation in polyamine levels in *Pten*$^{i\Delta EC}$ isolated EC cultures and in *Pten*$^{i\Delta EC}$ WAT (Fig. 6h,i and Extended Data Fig. 9a,b). Moreover, elevated polyamine levels were observed in the supernatant of *Pten*$^{i\Delta EC}$ EC, in agreement with their secreted nature (Fig. 6j).

Polyamines activate β-ADRs to promote lipolysis. We next ascertained the role of polyamines in regulating WAT biology. Supplementation of ^{13}C-spermidine in adipocyte cultures showed that this polyamine was efficiently taken up (Fig. 7a). Increased lipolysis in *Pten*$^{i\Delta EC}$ WAT is dependent on β-ADR activation (Fig. 6d) and polyamines reportedly promote β-ADR activity[47]. Hence, we tested whether polyamines promoted the release of adipose FFA in a β-ADR-dependent fashion. Supplementation of polyamines to WAT explants increased lipolysis, an effect that was prevented by propranolol (Fig. 7b and Extended Data Fig. 10a). Also, we showed that polyamines stimulated lipolysis in freshly isolated primary adipocyte cultures in a β-ADR receptor-dependent manner (Fig. 7c and Extended Data Fig. 10b). β-ADR receptors signal through PKA activation and cyclic AMP production[29] and we could confirm that spermidine increased the production of intracellular cAMP in adipocytes[47] (Fig. 7d and Extended Data Fig. 10c). The capacity of propranolol to block the action of spermidine on β-ADR in WAT explants suggests that there is sufficient natural agonist in the assay (tissue-intrinsic sympathetic innervation) to sustain a basal β-ADR activity. Indeed, we detected the presence of these agonists by liquid chromatography–mass spectrometry (LC–MS) in the adipose tissue explants employed in our assays (Extended Data Fig. 10d). Overall, our data suggest that polyamines are angiocrine mediators of lipolysis through the regulation of β-ADR activity in adipocytes.

To demonstrate that angiocrine polyamines are key regulators of adiposity, we evaluated the effect of polyamine supplementation in vivo. The administration of spermidine to diet-induced obese mice for 6 weeks tempered the obesogenic phenotype induced by HFD, selectively reduced WAT mass and adipocyte size and improved glucose tolerance (Fig. 7e–j and Extended Data Fig. 10e–g). Also, polyamine supplementation significantly reduced food intake in mice (Extended Data Fig. 10h). To rule out that the effect of polyamines was not solely due to reduced food intake, we performed pair-feeding studies in HFD-fed mice. After 10 weeks on HFD, vehicle-treated animals were heavier than the ones supplemented with spermidine, but when the control group was pair-fed with spermidine-treated mice, the differences in body weight were partially maintained (Extended Data Fig. 10i). We also examined whether obesity states are associated with reduced WAT polyamine levels. Notably, WAT from both mice subjected to HFD and humans with obesity exhibited reduced polyamine content (Fig. 7k,l, Extended Data Fig. 10j and Supplementary Table 4).

AMD1 inhibition restores reduced adiposity in *Pten*$^{i\Delta EC}$ mice. We have previously identified a molecular link between the PI3K pathway and polyamine biosynthesis in prostate cancer[46]. Activation of mTOR complex 1 (mTORC1) as a consequence of *Pten* deletion results in elevated Amd1 protein levels and the elevation of decarboxylated dcSAM, thus promoting the synthesis of polyamines[46]. As shown in Extended Data Fig. 9a,b, dcSAM was significantly increased in cultured ECs and WAT from *Pten*$^{i\Delta EC}$ mice. In agreement, we confirmed that Amd1 protein levels, but not mRNA gene expression, were higher in *Pten*-null ECs (Fig. 8a and Extended Data Fig. 10k), an effect that was counteracted by the inhibition of mTORC1 with rapamycin (Extended Data Fig. 10l,m).

To address the relevance of Amd1 activity in the phenotype elicited upon endothelial *Pten* loss and in the absence of a conditional *Amd1* knockout mouse model, we took advantage of a selective inhibitor of this enzyme, SAM486A. We confirmed that the conditioned medium from *Pten*-deficient ECs pre-treated with SAM486A was unable to increase lipolysis in WAT explants (Fig. 8c,d). In addition, explants from *Pten*$^{i\Delta EC}$ mice treated with SAM486A exhibited lower lipolytic rates (Fig. 8e) and *Pten*$^{i\Delta EC}$ mice treated with SAM486A demonstrated greater body weight (Fig. 8f) and adiposity than vehicle-treated counterparts (Fig. 8g–k). Together, these data uncover polyamines as angiocrine metabolic regulators of lipolysis and adiposity under the control of endothelial PTEN.

Discussion

ECs have been long studied as structural components of blood vessels with a bystander role in systemic metabolic homeostasis.

Fig. 5 | Lipid oxidation is essential for *Pten*-null EC proliferation. a,**b**, Expression of lipid catabolic genes analyzed by qPCR and normalized by *mL32* gene expression in eWAT (**a**) endothelium from control *Ribotag*^{iHAEC} and *Pten*$^{i\Delta EC}$-*Ribotag*^{iHAEC} (control *Ribotag*^{iHAEC} $n=5$; *Pten*$^{i\Delta EC}$-*Ribotag*^{iHAEC} $n=9$) and cultured primary adipose ECs (**b**) from control ($n=5$) and *Pten*$^{i\Delta EC}$ mice ($n=4$). **c**, FAO analysis in control ($n=7$) and *Pten*$^{i\Delta EC}$ ($n=8$) adipose ECs. **d**, Oxygen consumption rate (OCR) in control ($n=4$) and *Pten*$^{i\Delta EC}$ ($n=5$) adipose EC cultured in lipid-enriched medium. **e**, Quantification of OCR in control and *Pten*$^{i\Delta EC}$ adipose EC in lipid-enriched medium (control $n=4$; *Pten*$^{i\Delta EC}$ $n=5$). **f**, OCR in control and *Pten*$^{i\Delta EC}$ adipose EC in non-lipid-enriched medium ($n=5$ per group). **g**, OCR quantification from control and *Pten*$^{i\Delta EC}$ adipose EC in non-lipid-enriched medium ($n=5$ per group). **h**, Cell proliferation assessment by crystal violet in adipose EC from control and *Pten*$^{i\Delta EC}$ in the presence or absence of etomoxir (control $n=6$; *Pten*$^{i\Delta EC}$ $n=8$). **i**, Representative whole-mount images of IB4-stained blood vessels (red) in flat-mounted eWAT from control and *Pten*$^{i\Delta EC}$ mice treated either with vehicle or etomoxir for 5 weeks. **j**, Quantification of IB4-positive area in control and *Pten*$^{i\Delta EC}$ eWAT after 5 weeks of vehicle or etomoxir administration (control – vehicle $n=7$; control – etomoxir $n=6$; *Pten*$^{i\Delta EC}$ – vehicle $n=6$; *Pten*$^{i\Delta EC}$ – etomoxir $n=6$). **k**, eWAT pad weight in control and *Pten*$^{i\Delta EC}$ mice treated with vehicle or etomoxir for 5 weeks (control – vehicle $n=15$; control – etomoxir $n=9$; *Pten*$^{i\Delta EC}$ – vehicle $n=11$; *Pten*$^{i\Delta EC}$ – etomoxir $n=10$). Data represent mean ± s.e.m. Samples represent biological replicates. Statistical analysis was performed by the two-sided Mann–Whitney *U*-test (**a**–**c**,**e**,**h**,**j**) and two-way ANOVA with Bonferroni correction (**h**).

Our data, together with others[2], challenge this view and show that manipulation of EC biology influences systemic metabolism with pathobiological implications. We provide evidence that EC function modulates adiposity through angiocrine production of polyamines acting directly on adipocytes in a paracrine fashion (Fig. 8l). Remarkably, we demonstrate that ECs exploit the metabolic angiocrine communication mode to stimulate the release of FFAs from adipocytes to sustain cell proliferation and promote vascular

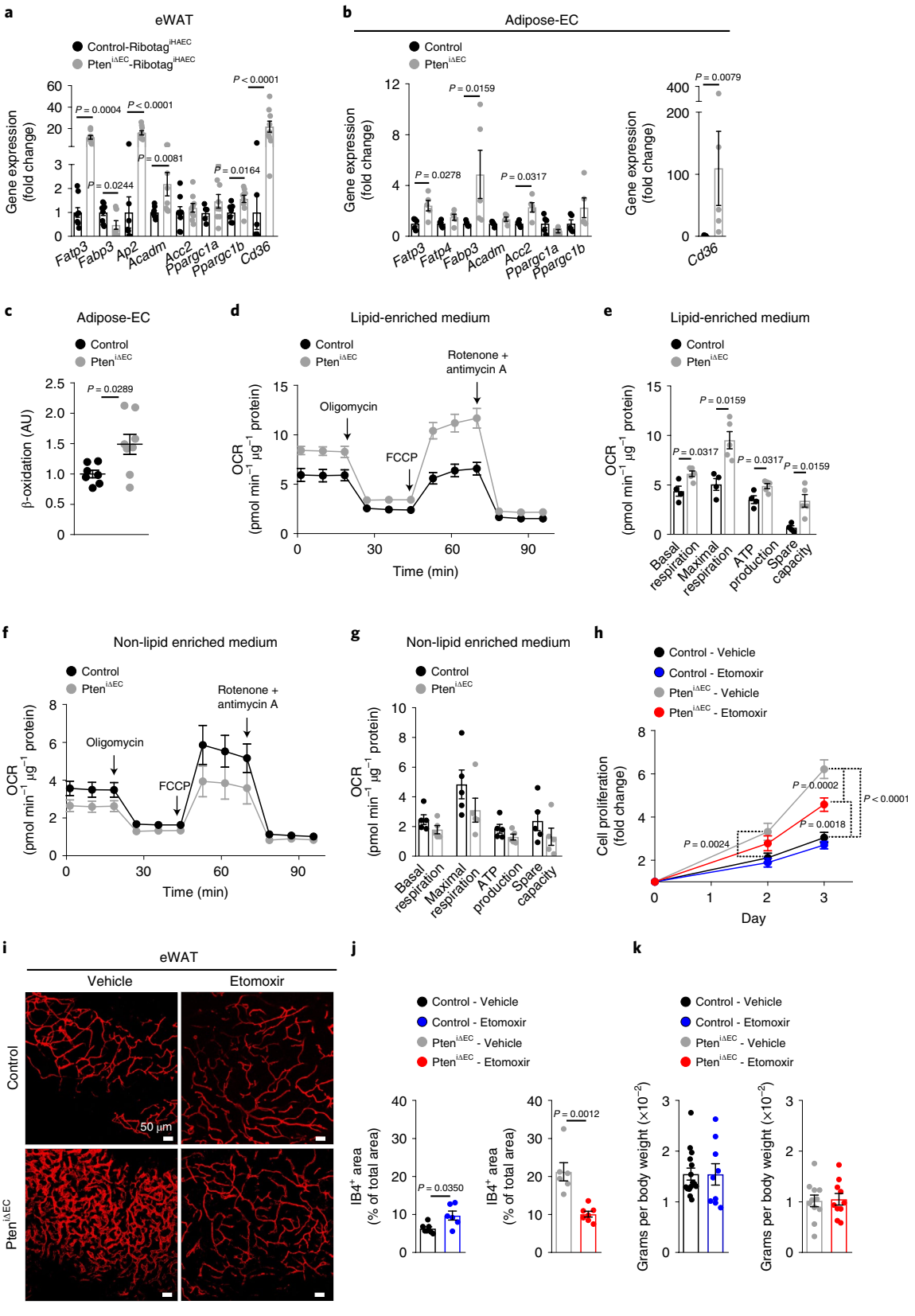

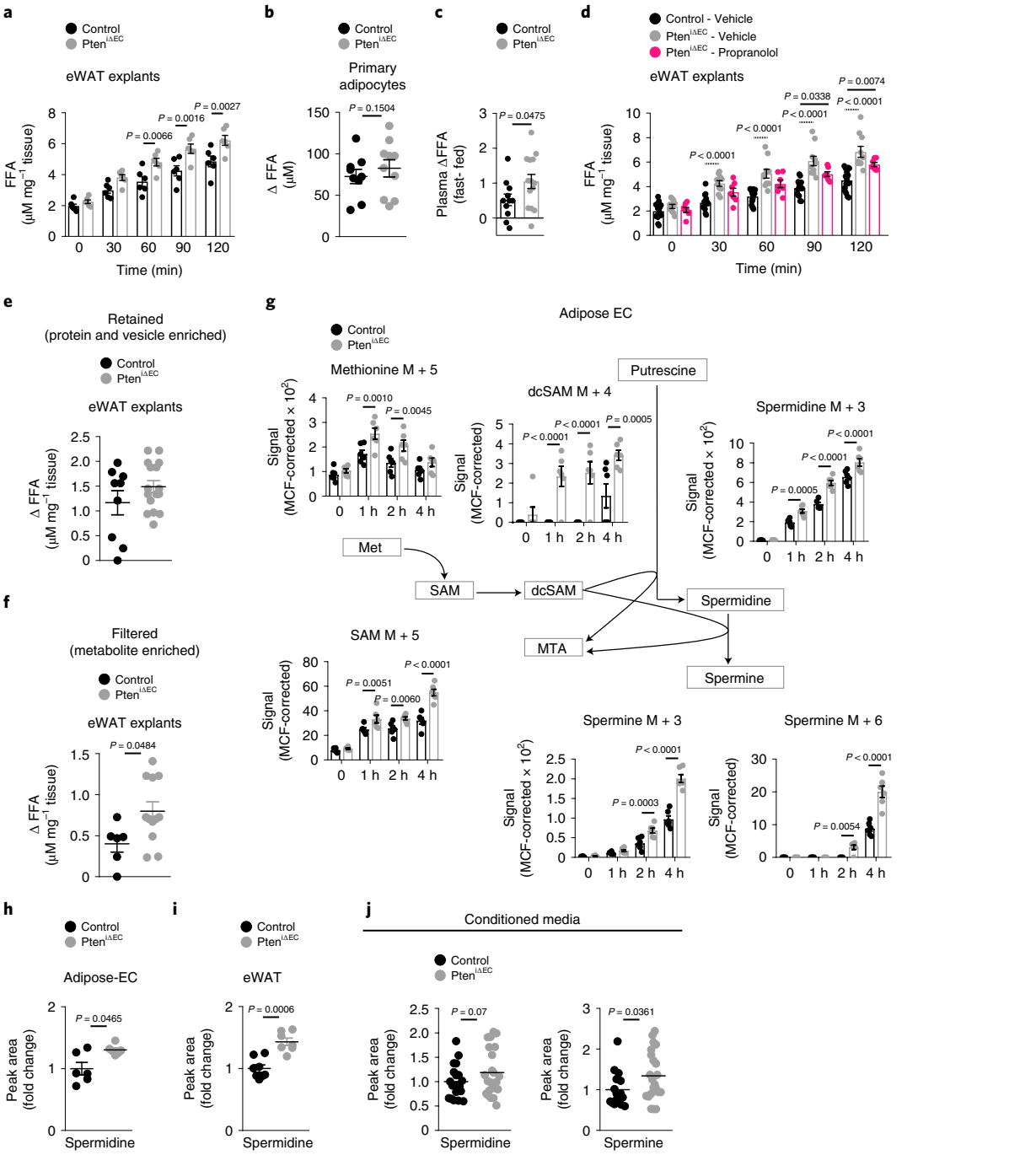

Fig. 6 | Endothelial-derived polyamines stimulate lipolysis. a, FFA release from eWAT explants of control and *Pten*$^{i\Delta EC}$ mice in basal conditions ($n = 6$ per group). **b**, Release of FFAs in primary adipocytes, shown as the difference between FFA levels at min 180 and min 0 (ΔFFA) in primary adipocyte cultures following incubation with conditioned medium from control and *Pten*$^{i\Delta EC}$ adipose ECs (control $n = 9$; *Pten*$^{i\Delta EC}$ $n = 10$). **c**, Levels of FFA in serum of control and *Pten*$^{i\Delta EC}$ mice, shown as the difference between overnight fast and fed ad libitum conditions (control $n = 11$; *Pten*$^{i\Delta EC}$ $n = 14$). **d**, FFA release from eWAT explants of control and *Pten*$^{i\Delta EC}$ mice after 4 d of treatment with either vehicle or propranolol (pan β-ADR inhibitor; control vehicle $n = 16$; *Pten*$^{i\Delta EC}$ vehicle $n = 10$; *Pten*$^{i\Delta EC}$ – propranolol $n = 7$). **e**, Increase in FFA release of eWAT explants from wild-type mice following incubation with the retained fraction (protein- and vesicle-enriched) of conditioned medium from adipose ECs from control and *Pten*$^{i\Delta EC}$ mice (control $n = 9$; *Pten*$^{i\Delta EC}$ $n = 16$). **f**, Increase in FFA release from eWAT explants of wild-type mice following incubation with the metabolite-enriched fraction (filtered fraction) of conditioned medium from control and *Pten*$^{i\Delta EC}$ ECs (control $n = 6$; *Pten*$^{i\Delta EC}$ $n = 12$). **g**, Incorporation of carbon-13 (^{13}C) from ^{13}C-U_5-methionine (2-h and 4-h pulse) into metabolites related to polyamines biosynthesis in adipose ECs from control and *Pten*$^{i\Delta EC}$ mice ($n = 6$ per group). MET, methionine; SAM, S-adenosylmethionine; dcSAM, decarboxylated S-adenosylmethionine; MTA, 5′ methylthioadenosine. **h**,**i**, Spermidine levels in adipose ECs (**h**) (control $n = 6$; *Pten*$^{i\Delta EC}$ $n = 6$) and in whole tissue eWAT (**i**) (control $n = 8$; *Pten*$^{i\Delta EC}$ $n = 7$) measured by LCMS. **j**, Spermidine (control $n = 20$; *Pten*$^{i\Delta EC}$ $n = 23$) and spermine (control $n = 17$; *Pten*$^{i\Delta EC}$ $n = 22$) levels in conditioned medium from adipose ECs from control and *Pten*$^{i\Delta EC}$ mice measured by LCMS. Total number of samples control (17 and 20) and *Pten*$^{i\Delta EC}$ (22 and 23) correspond to independent EC cultures from eight WAT depots of each genotype. Data represent mean ± s.e.m. Samples represent biological replicates. Statistical analysis was performed by the two-sided Mann–Whitney *U*-test (**a**,**c**,**f**), one-sided Mann-Whitney *U*-test for hypothesis-driven analyses (**b**,**h**–**j**), *t*-test (**g**) and one-way ANOVA with Bonferroni correction (**d**).

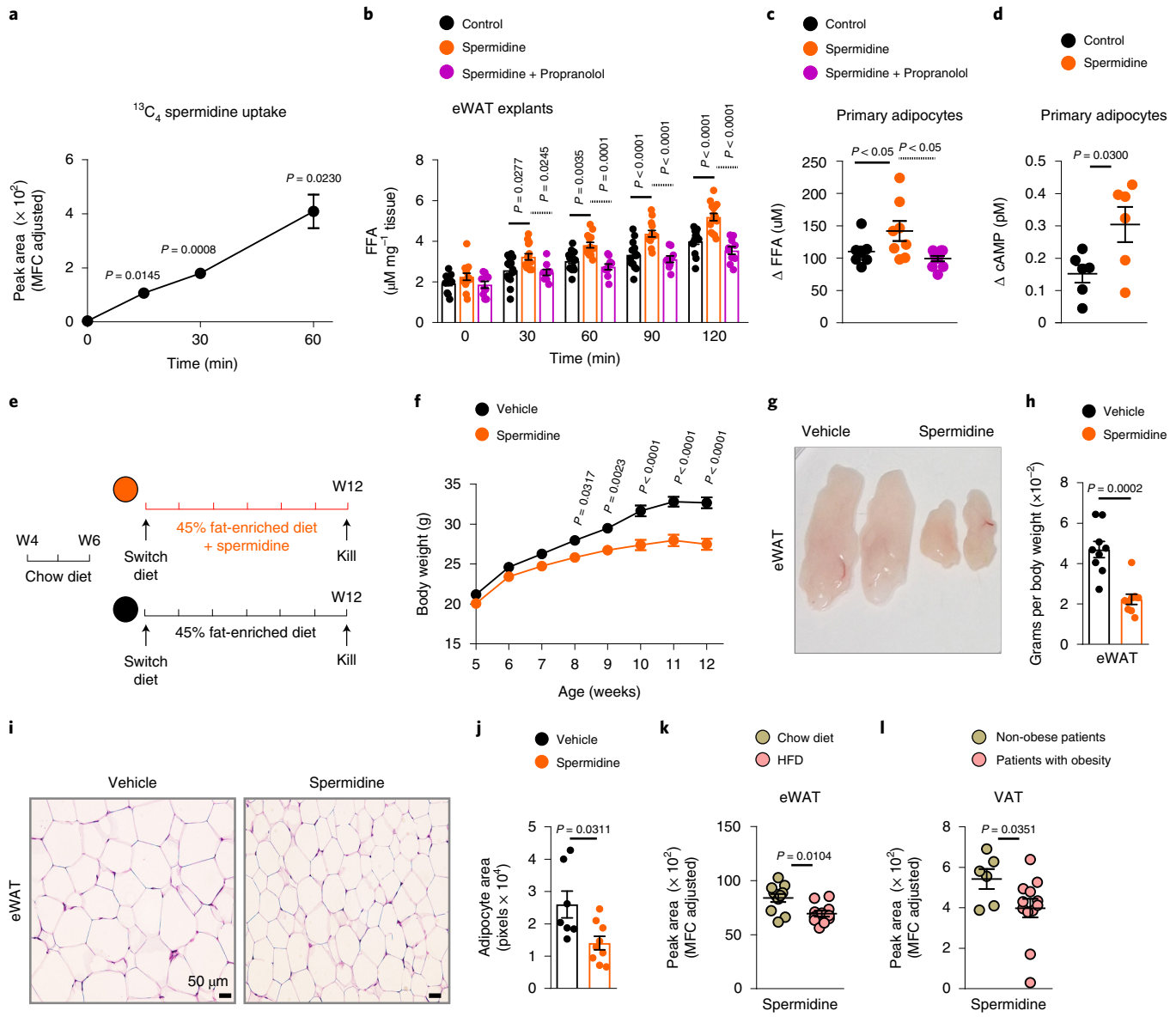

Fig. 7 | Polyamines fine-tune β-ADR-dependent lipolysis. a, $^{13}C_4$ spermidine uptake from wild-type primary adipocytes ($n=3$) at the indicated times. **b**, FFA release of wild-type eWAT explants supplemented with spermidine or spermidine in combination with propranolol (control $n=14$; spermidine $n=14$; spermidine + propranolol $n=10$). **c**, Release of FFA, shown as the difference between FFA levels at min 180 and min 0 (ΔFFA) in adipocyte cultures supplemented with spermidine alone or in combination with propranolol (control $n=8$; spermidine $n=8$; spermidine + propranolol $n=10$). **d**, Production of cAMP, shown as the difference between cAMP levels at min 15 and min 0 (ΔcAMP) in primary adipocytes following spermidine supplementation (control $n=6$; spermidine $n=6$). **e**, Experimental design of spermidine treatment in wild-type mice exposed to HFD. **f**, Body weight curves of wild-type mice fed with HFD and treated with vehicle or spermidine (vehicle $n=9$; spermidine $n=10$). **g**, representative macroscopic images of eWAT. **h**, eWAT pad weight ($n=9$). **i**, Representative histological sections from eWAT. **j**, Quantification of adipocyte area in eWAT (vehicle $n=7$; spermidine $n=9$) of wild-type mice fed with HFD and treated with vehicle or spermidine. **k**,**l**, Spermidine levels in whole-tissue eWAT (**k**) from chow and HFD wild-type mice (chow $n=11$, HFD $n=11$) and omental VAT (**l**) from non-obese and obese human individuals (non-obese $n=6$, obese $n=12$) measured by LC–MS. Data represent mean ± s.e.m. Samples represent biological replicates. Statistical analysis was performed by the two-sided Mann–Whitney *U*-test (**h**,**j**,**k**), one-sided Mann–Whitney *U*-test for hypothesis-driven analyses (**l**), *t*-test for paired groups (**a**,**d**), one-way ANOVA with Bonferroni correction (**b**,**c**) and two-way ANOVA with Bonferroni correction for correction for three or more unmatched groups (**f**).

growth. By doing so, ECs protect WAT from pathological expansion in the context of obesity.

Angiocrine is a term used to define endothelial-derived paracrine signals that mediate parenchymal function and regenerative functions in an organ-specific manner[32–34,48]. Yet, little is known about the intercellular endothelial-to-adipocyte communication. We uncover that ECs communicate with adipocytes through metabolites, the so-called polyamines. Other examples of angiocrine-related organ regulation include liver and lung regeneration, neuronal stem cell function, tumor angiogenesis and heart development[32,49–54]; however, angiocrine signals in those contexts are of a protein nature. Recent evidence has recognized that metabolites produced and secreted by ECs also function as angiocrine signals[35,55]. This is the case for muscle and retinal ECs, which secrete lactate, a product of glycolysis[35,55].

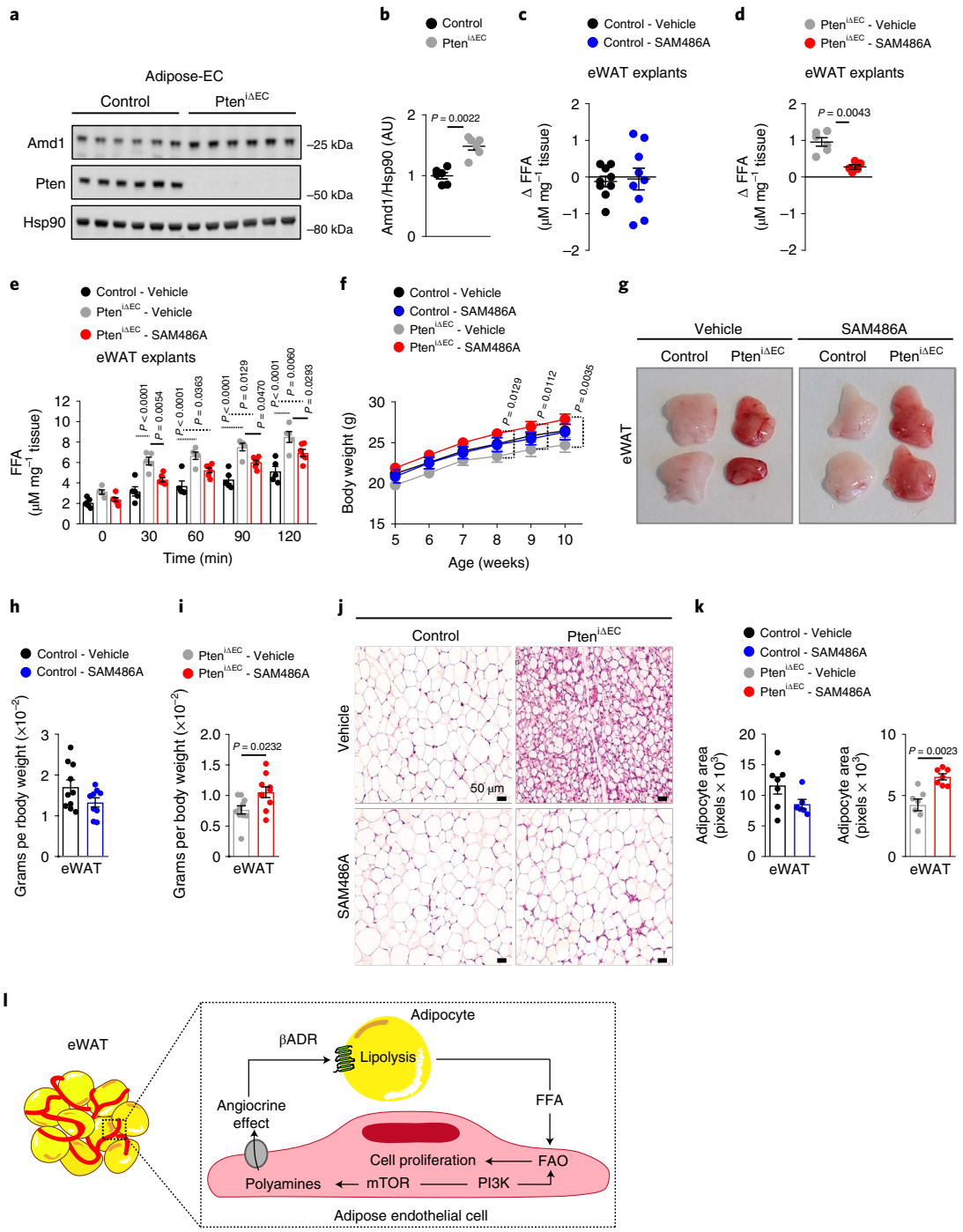

Fig. 8 | Pharmacological modulation of Amd1 regulates adiposity. a, Immunoblot analysis of Amd1 and Pten in control and *Pten*$^{i\Delta EC}$ adipose ECs lysates from control and *Pten*$^{i\Delta EC}$ mice. **b**, Quantification of Amd1 signal obtained in immunoblots shown in **a** ($n=6$ per group). **c**,**d**, FFA release of wild-type WAT explants (shown as ΔFFA at min 180) following incubation with conditioned medium from control (**c**) and *Pten*$^{i\Delta EC}$ (**d**) adipose ECs pre-treated with vehicle or SAM486A (control – vehicle $n=9$; control – SAM486A $n=9$; *Pten*$^{i\Delta EC}$ – vehicle $n=6$; *Pten*$^{i\Delta EC}$ – SAM486A $n=5$). **e**, FFA release of explants from control mice treated with vehicle ($n=5$) or *Pten*$^{i\Delta EC}$ mice treated with vehicle or SAM486A for 4 d (vehicle $n=5$; SAM486A $n=6$). **f**, Body weight curves ($n=10$ per group). **g**, Representative macroscopic images of eWAT. **h**,**i**, eWAT pad weight (control – vehicle $n=10$; control – SAM486A $n=9$; *Pten*$^{i\Delta EC}$ – vehicle $n=10$; *Pten*$^{i\Delta EC}$ – SAM486A $n=10$). **j**, representative histological sections from eWAT. **k**, Quantification of adipocyte area (control – vehicle $n=7$; control – SAM486A $n=6$; *Pten*$^{i\Delta EC}$ – vehicle $n=7$; *Pten*$^{i\Delta EC}$ – SAM486A $n=7$) in eWAT of control and *Pten*$^{i\Delta EC}$ mice treated with vehicle or SAM486A for 5 weeks. **l**, Schematic representation of the proposed model illustrating how molecular reprogramming of adipose ECs generates both the means (polyamine-regulated lipolysis in WAT) and the demand for nutrients (increased capacity to catabolize fatty acids) to support vascular growth, in a bidirectional angiocrine communication with WAT. These data demonstrate an important role of angiocrine metabolic signals in tissue homeostasis. Data represent mean ± s.e.m. Samples represent biological replicates. Statistical analysis was performed by the two-sided Mann–Whitney *U*-test for comparing two unmatched groups (**b**,**h**,**i**,**k**), one-sided Mann–Whitney *U*-test for hypothesis-driven analyses (**c**,**d**), one-way ANOVA with Bonferroni correction for three or more unmatched groups (**e**) and two-way ANOVA for two or more matched groups (**f**).

However, this is not surprising given that ECs are largely glycolytic cells[56]. A notable observation from these studies is that lactate does not directly interact with parenchymal cells, but it engages macrophages, which act as mediators of tissue regeneration and angiogenesis[35,55]. In contrast, we identify that endothelial-derived polyamines, upon secretion, directly stimulate lipolysis in adjacent adipocytes; thus, demonstrating that angiocrine metabolic signaling directly regulate parenchyma function.

A remarkable result from our study is that loss of *Pten* in the endothelium result in a WAT-restricted phenotype. This is consistent with the observation that ECs specialize in each type of organ to fulfill tissue-specific tasks by cues that are essential for organ function[33]. Given that *Pten*-null cells primarily use lipids to proliferate and that WAT serves as a reservoir of lipids, our results suggest that the environmental milieu educates EC behavior. This would also explain why in BAT, a tissue with a mild accumulation of lipids, *Pten*-null ECs exhibit a moderate increase in proliferation. While at present it is not clear how organotypic differences between ECs emerge, our data call for considering the uniqueness of each environmental milieu as a key determinant of this EC specialization. We propose that understanding which signals from each organ microenvironment regulate the unique properties of ECs could offer tissue-specific vascular therapies not only to repair malfunctional or degenerative tissues, but also to improve their homeostatic function.

The exhaustive pathophysiological analyses of the $Pten^{i\Delta EC}$ mice included here have allowed us to identify a causal relationship between reduced body weight and adiposity with enhanced local metabolic rate in WAT and increased usage of FFA by $Pten^{i\Delta EC}$ ECs. While we cannot rule out that the adipocytes contribute to the enhanced basal metabolic rate in $Pten^{i\Delta EC}$ mice, our data support the concept that adipose $Pten^{i\Delta EC}$ ECs actively contribute to energy consumption by lipid oxidation. This is consistent with the observation that ECs can use lipids to sustain a proliferative phenotype[26,57,58]. We believe that the observation that loss of endothelial *Pten* in BAT also results in a mildly enhanced vascularization relates to the lipid availability in this tissue. This, in fact, further supports the conclusion that *Pten* deletion makes ECs prone to proliferate in the presence of fatty acids, which represents a microenvironmental prerequisite for these cells.

We have not been able to confirm a role for improved BAT function or WAT browning in the phenotype of $Pten^{i\Delta EC}$ mice. This is surprising given that VEGF-related enhanced angiogenesis in iWAT leads to improved systemic metabolic health by stimulating browning in this tissue[22–24]. Although the reason for this difference is not clear, collectively these studies reinforce the notion that enhanced vascularity improves WAT function. This fits with recent studies showing that age-dependent organ decline is associated with reduced vessel density[59,60] and that VEGF signaling prevents age-associated capillary loss, improves organ perfusion and function and extends life span[60].

Polyamines are small polycations that are considered instrumental in proliferative cells[38]. Indeed, we show that polyamines are produced in the proliferative adipose endothelium and extrapolate evidence acquired in cancer studies to the endothelial field[46]. We demonstrate that the connection between the PI3K/mTORC1 pathway and AMD1 activity is operative in ECs. Notably, beyond the role of these metabolites in cell proliferation, we show that they function as paracrine regulators of adipocyte biology. A follow-up question would be to identify whether polyamines are angiocrine mediators in any ECs that undergoes proliferation or whether they selectively function as angiocrine mediators of adipose ECs. A critical finding from our study is that EC-derived secreted polyamines regulate the activity of β-ADRs, a concept for which there was solely isolated evidence to date[47,61,62]. However, a relevant question that remains is whether polyamines require the presence of β-ADR ligands to promote the activation of the receptor, an idea the has been proposed in specific experimental settings[47]. We observed that both supplemented polyamines and conditioned medium from *Pten*-deficient ECs activate the release of FFA in WAT explants, which contain detectable levels of β-ADR ligands. However, similar experiments performed in primary adipocyte cultures showed that while polyamine supplementation recapitulated the elevated release of FFA, the conditioned medium from *Pten*-deficient ECs had limited differential lipolytic activity compared to that of wild-type ECs. Taken together, our results suggest that the presence of β-ADR ligands enhances the capacity of polyamines to promote lipolysis. In the absence of these ligands (such as adipocyte cultures) the lipolytic activity of *Pten*-deficient EC-conditioned medium would lose potency, whereas supplemented polyamines in this assay would retain activity, probably owing to their elevated relative abundance in the assay. Assuming that the conditioned medium best recapitulates the secreted polyamine conditions, we propose that polyamines function as fine-tuners of canonical β-ADR signals. Of note, our data agree with previous observations showing that exogenous administration of spermidine regulates lipid metabolism and in turn ameliorates the WAT pathophysiological response to HFD[63]. This provides further support that polyamines and in particular spermidine, may open new therapeutic avenues to treat obesity.

Taken together, we uncover an unappreciated mode of communication between ECs and adipocytes with implications for systemic metabolism. Our data provide evidence that this mode of communication is disrupted in obesity, thus, opening further research avenues to comprehend and treat this disease. Also, we propose that understanding the extent of the contribution of polyamines to adrenergic signaling-driven cellular responses may be important in many other biological contexts.

Methods

All our research compiles with the relevant ethical regulation. Experiments pertaining to mouse work were conducted in accordance with the guidelines and laws of the Catalan Departament d'Agricultura, Ramaderia i Pesca (Catalunya, Spain) and were approved by the Ethics Committees of Institut d'Investigació Biomèdica de Bellvitge. The Hospital Clinical of Barcelona Ethical Committee approved the human studies and all study participants provided informed consent to donate tissue samples.

Reagents. All reagents used in this work are listed in Supplementary Tables 1, 2 and 3, including commercial references and experimental dosage.

Mice. Mice were maintained under specific-pathogen-free conditions and kept in individually ventilated cages. Mice were fed ad libitum either with chow diet or HFD (45% fat-enriched diet). The transgenic mouse colony was kept under mixed background of C57BL/6J and 129. $Pten^{flox}$ mice[15] were crossed into the transgenic mice expressing the tamoxifen-inducible recombinase CreER under the control of *Pdgfb* promoter (*PdgfbiCreER*) transgenic mice[16] or into the control of Cdh5 promoter (*Cdh5-CreER*^{T2})[18]. Only male mice were used for our studies. For isolation of EC-specific actively translating mRNA, $Ribotag^{flox}$ mice ($Rpl22^{tm1.1Psam}$)[17] were crossed with *Pdgfb-iCre-ER* ($Ribotag^{iHAEC}$) and $Pten^{i\Delta EC}$ ($Pten^{i\Delta EC}$-$Ribotag^{iHAEC}$). Cre activity and gene deletion were induced by intraperitoneal (i.p.) injection of 4-OHT at 25 mg (2.5 µl of a 10 mg ml^{-1} solution in absolute ethanol) in pups at postnatal day (P)2 and P3 and tissues were collected at 5 and 12 weeks of age. In adult mice, gene deletion was induced by i.p. injections of tamoxifen (75 mg kg^{-1}; resuspended in peanut oil) at 8 or 18 weeks of age for three alternate days. Both Cre-positive and -negative mice were treated with 4-OHT or tamoxifen. For combined EC-specific loss-of-function of *Pten* and *Ppargc1b*, we crossed $Pten^{flox}$ mice[15] with $Pgc1\beta^{flox}$ mice[28] and *PdgfbiCreER*[16] mice. For pharmacological rescue studies, control and $Pten^{i\Delta EC}$ mice were treated with vehicle (saline), etomoxir (25 mg kg^{-1}) or SAM486A (5 mg kg^{-1}) from 5 to 10 weeks of age. For explants, mice were treated for 4 d with vehicle (saline), SAM486A (5 mg kg^{-1}), spermidine (20 mg kg^{-1}) or propranolol (20 mg kg^{-1}). Etomoxir and SAM486A in vivo experiments were planned by choosing a dose, route of administration and drug regimen previously published by us[27,46]. For spermidine treatment, wild-type C57BL/6J mice (purchased from Charles River) were fed with HFD and were treated with vehicle or spermidine (20 mg kg^{-1}) from 6 to 12 weeks of age daily, excluding weekends. Of note, the spermidine supplementation strategy 20 mg kg^{-1} is within physiological ranges of spermidine supplementation[43,64]. All in vivo experiments of our study, including chow and HFD conditions, were performed

without altering the normal presence of dietary polyamines. Before starting in vivo experiments, mice were weighed and homogenously distributed in experimental groups. All other criteria were not considered and as such, were randomized.

Human cohort. We studied omental VAT from morbid patients with obesity (body mass index (BMI) > 35) undergoing bariatric surgery and non-obese individuals (BMI < 30) undergoing abdominal surgery at the Hospital Clinic of Barcelona. Participant information including sex, number, BMI and age (Supplementary Table 4). Participants of the study did not receive any compensation.

RiboTag, RNA extraction, cDNA synthesis and qPCR. Enrichment of the active translating RNA was achieved by immunoprecipitation (IP) of ribosomes via hemagglutinin A (HA) as described[65]. RNA was isolated from tissues, EC lysates and Ribotag immunoprecipitates using RNeasy Plus Mini and RNeasy Micro kit, respectively, following manufacturer's instructions. To obtain complementary DNA, reverse transcription was performed from 500 ng of RNA by using High-Capacity cDNA Reverse Transcription kit (Applied Biosystems). For quantitative PCR, a LightCycler 480 System (Roche) was used with LightCycler 480 SYBR Green I Master kit (Roche) or a QuantStudio 5 System (Applied Biosystems) with TaqMan Universal PCR Master Mix (Applied Biosystems). Specific primers detailed on Supplementary Table 2. *mL32* or *Hprt1* were used as housekeeping genes.

Vascular density analysis. Tissues were cut into 3-mm^3 cubes, permeabilized for 1 h with PBS + 1% Triton X-100 and blocked with blocking buffer (1× PBS + 0.3% Triton X-100 + 5% goat serum) for 2 h at room temperature. Primary and secondary antibodies (Supplementary Table 3) diluted in blocking buffer were incubated overnight at room temperature, with over-day washings with PBS + 0.3% Triton X-100 after both incubations. Mouse WAT pads were stained with Alexa-conjugated isolectin B4 (IB4). Human WAT pads were stained with anti-CD31 antibody. To study the vasculature of BAT, muscle, liver, heart and brain, we used cryosection immunostaining. Freshly isolated tissues were fixed overnight in 4% paraformaldehyde, washed in PBS, dehydrated in 30% sucrose overnight and embedded in OCT. BAT (14 µm), muscle, heart, brain (10 µm) and liver (5 µm) cryosections were cut using the Cryostat (Leica Microsystems). BAT sections were blocked with 1× PBS 0.3% Triton X-100 + 5% goat serum for 1 h at room temperature, followed by incubation with Alexa-conjugated IB4 overnight at 4 °C. Muscle, liver, heart and brain sections were incubated in Tris-EDTA solution (0.1 M EDTA + 0.001 M Tris-base + 0.05% Tween 20) in a steamer for 30 min. After cooling down, sections were blocked with 1× PBS + 5% donkey serum + 0.4% Triton X-100 for 1 h at room temperature, followed by incubating overnight at 4 °C with anti-CD31 antibody and with secondary antibody 1 h at room temperature (Supplementary Table 3) in blocking solution. To analyze vessel area and proliferation, images were taken with a Leica SP5 laser-scanning confocal microscope (Leica Application Suite) or Nikon 80i microscope (NIS-Elements) using ×20 and ×40 objectives. Confocal images are maximal intensity z-stack projections and images were processed using Volocity, Fiji and Adobe Photoshop CS5. Vessel density was quantified by measuring the IB4-positive or CD31-positive area using ImageJ software. Endothelial branch points were quantified in four images per each sample (taken with ×40 oil immersion objective) and represented as an average.

Histology analysis. The 5-µm thick paraffin sections were stained with hematoxylin/eosin and mounted with DPX mounting medium. Adipocyte area was calculated with the Adiposoft tool of ImageJ software. Fibrosis was evaluated by Trichrome Stain kit following manufacturer's instructions. Cell death was evaluated by immunostaining of cleaved caspase-3 in paraffin sections, following the standard protocol. Briefly, antigen retrieval was performed with citrate buffer and permeabilization with PBS + 0.2% Tween 20, primary antibody was incubated overnight at 4 °C and secondary 2 h at room temperature (Supplementary Table 3). Samples were mounted with Shandon Immu-Mount. Images were taken with a Nikon 80i microscope using a ×20 objective.

Glucose tolerance test, insulin tolerance test and HOMA-IR index. GTT and ITT were performed in 6-h fasted mice. Both compounds were i.p. injected, glucose (1.5 g kg^{-1}) and insulin (0.75 UI kg^{-1}) and blood glucose was monitored for 90–120 min. HOMA-IR index was calculated applying the following formula: (fasting glucose (mg dl^{-1}) × fasting insulin (mU l^{-1})) / 405. Insulin was measured with Ultra-Sensitive Mouse Insulin ELISA kit following manufacturer's instructions.

Daily food intake. Mice were single housed, acclimatized for 1 week before study and a weighed amount of food was provided. Food intake was measured for five consecutive days at 8 and 12 weeks of age. Pair feeding was carried out to determine the extent to which the body weight-reducing effect of spermidine treatment was the consequence of changes in food intake. All mice were individualized during the pair-feeding protocol. The average food intake of the spermidine-treated group was daily measured between 9:00 and 10:00. Subsequently, the pair-fed group was offered the same amount of food eaten by spermidine-treated mice on the previous day.

Body composition, Indirect calorimetry, locomotor and thermogenic activity. Body weight and discrete adipose tissue pad mass were measured using a precision scale. Whole body composition was measured using nuclear magnetic resonance imaging (Whole Body Composition Analyzer; EchoMRI). Indirect calorimetry and locomotor activity was assessed using a TSE LabMaster modular research platform (TSE Systems) as previously described[66,67]. Briefly, mice were acclimatized for 24 h into test chambers and monitored for additional 48 h. O_2 consumption and CO_2 production were measured every 45 min during 48 h, to indirectly determine EE. Locomotor activity was determined using a multidimensional infrared light beam system with the parameters defined by the LabMaster software. These analyses were performed at 7 weeks of age, before body weight differences between control and *Pten*$^{i\Delta EC}$ mice were apparent. Heat production was visualized using a high-resolution infrared camera (FLIR PM280; FLIR Systems), as previously described[68].

Western blot. Cell lysis, SDS–PAGE and immunoblot were performed as previously described[14]. Antibodies used are listed in Supplementary Table 3. Quantification of band intensities by densitometry was carried out using ImageJ software.

Mitochondrial respiration. Mitochondrial respiration was assessed in freshly isolated eWAT, iWAT, muscle and liver by high-resolution respirometry in an Oroboros Oxygraph-2k system (Oroboros Instruments) as previously reported[69]. LEAK respiration was measured by the addition of NADH-linked substrates (complex I linked) malate (2 mM) and pyruvate (5 mM) in the absence of ADP. OXPHOS state was measured by adding ADP + $MgCl_2$ (5 mM) and cytochrome C (10 µM), followed by the subsequent addition of glutamate (10 mM) (NADH-linked pathway) and succinate (10 mM) (convergent electron flow through both, NADH- and succinate-linked pathways). FCCP (0.5 µM) was titrated to evaluate the maximal capacity of the electron transfer system (ETS; CI + CII). Finally, rotenone (0.5 µM) was used to inhibit CI and measure ETS fueled by succinate-linked pathway. Oxygen flux values were expressed relative to tissue wet weight per second (pmol O_2 mg^{-1} s^{-1}). Residual oxygen consumption (ROX) was determined by the inhibition of complex III adding antimycin A (2.5 µM) and this value was subtracted from O_2 flux as a baseline for all respiratory states.

Feces collection and analysis. Feces were collected from individually housed mice cages for 4 d, stored at −20 °C and desiccated at 60 °C before processing. Energy content in feces was measured using a calorimetric bomb in the Laboratorio de Nutrición Animal SERIDA (Villaviciosa, Spain). For triglyceride measurement, frozen feces samples were pulverized under liquid nitrogen and 100 mg portions were digested in 3 M KOH for 1 h at 70 °C, followed by overnight incubation at room temperature. Samples were diluted to a final concentration of 100 mg tissue in 500 µl Tris–HCl 50 mM before using triglycerides-LQ kit under manufacturer's instructions.

Primary ECs. Selection and culture conditions for adipose-derived and lung-derived ECs were as previously reported[14]. To assess cell proliferation 1 × 10^4 primary ECs were cultured in DMEM/F12 with 1% FBS, 2 mg ml^{-1} of AlbuMAX and half dose of EC growth factors in the presence or absence of etomoxir and measured by staining with crystal violet (0.1% in 20% methanol) at day 2 and 3 and normalized by day 0 values. For conditioned medium collection, 8 × 10^5 cells were cultured in 1 ml of DMEM 1 g l^{-1} glucose + 0.5% FFA-free BSA. After 4 h, medium was collected, centrifuged for 5 min at 300*g*, filtered with a 0.22 filter and kept at 4 °C (up to 2 d). When indicated, cells were pre-treated 24 h with vehicle (H_2O) or SAM486A (0.5 µM) in growing medium. For medium fractioning, 2.5 ml of medium was loaded into Amicon Ultra-4 filters (membrane PLBC Ultracel-3, 3 kDa) and centrifuged at 3,800*g*, 4 °C for 1 h. The flow-through (metabolite fraction) was collected and stored at 4 °C. The retained protein and vesicle fraction (150 µl), was washed with 2 ml of DMEM 1 g l^{-1} glucose, centrifuged again, diluted in 2 ml of DMEM 1 g l^{-1} glucose and stored at 4 °C. For Amd1 analysis, ECs were cultured for 24 h with vehicle (dimethylsulfoxide) or mTOR inhibitor (rapamycin, 1 µm). FAO was measured as previously described[70]. Briefly, after 4 h incubation of cells with [^{3}H] palmitate, medium was collected to analyze the released ^3H_2O formed during cellular oxidation, normalized to protein content. For glucose uptake, ECs were seeded 12 h before the experiment and then incubated in 900 µl of KRH buffer (20 mM HEPES, 136 mM NaCl, 4.7 mM KCl, 1.25 mM $MgSO_4$ and 1.25 mM $CaCl_2$) for 15 min at 37 °C and 100 µl of 10× START solution (1 mM 2-deoxyglucose and 5 µCi ml^{-1} [^{3}H]-2-deoxyglucose) were added afterward. Following 10 min of incubation at 37 °C, cells were washed and 1 ml of 0.03% SDS was added. Counts per minute (c.p.m.) were determined and normalized by mg of protein. To assess respiration, ECs were seeded in customized Seahorse 24-well plates. At 1 h before the assay, cells were maintained in XF Assay Medium Modified DMEM (Seahorse Bioscience) supplemented with 5 mM glucose in a non-CO_2 incubator and just before the assay, 10 µl of AlbuMAX were added (to a final concentration of 2 mg ml^{-1}). OCR was measured using the Seahorse XFe24 analyzer (Agilent) following the manufacturer's protocols. OCR was calculated by plotting the O_2 tension of medium as a function of time (pmol min^{-1}) and data were normalized by the protein concentration measured in each individual well. Calculations were performed using the Agilent Seahorse Wave Desktop software.

Primary adipocytes. The stromal vascular fraction (SVF) was isolated from iWAT depots of 6-week-old male mice. Differentiation was induced 48 h after cells reached confluence by adding the induction medium: DMEM complete with insulin (100 nM), dexamethasone (1 µM), 3-isobutyl-1-methylxanthine (IBMX) (0.5 mM) and rosiglitazone (1 µM). After 48 h, induction medium was replaced by DMEM complete + insulin (100 nM). Experiments were performed at day 8 of differentiation. Lipolysis was evaluated by measuring FFA release in differentiated adipocytes. Briefly, differentiated adipocytes were washed with 1× PBS and stimulated by (1) conditioned medium from control and *Pten*$^{i\Delta EC}$ ECs or (2) DMEM 1 g l^{-1} glucose + 0.5% FFA-free BSA ± 1 µM spermidine. DMEM 1 g l^{-1} glucose + 0.5% FFA-free BSA + 1 µM CL316243 (β-ADR agonist) was included in all assays as positive control. When stated, cells were pre-treated with 100 µM propranolol in DMEM complete + insulin (100 nM) during 2 h before the experiment. FFA release was measured at min 0 and min 180 and the difference between time points was calculated. FFA were measured using FFA assay HR-NEFA kit following manufacturer's instructions. cAMP was measured in primary adipocytes cell lysate after 15 min incubation with DMEM 1 g l^{-1} glucose + 0.5% FFA-free BSA ± 1 µM spermidine. Then, 10 µM forskolin was used as positive control. cAMP was measured using cAMP colorimetric assay, following manufacturer's instructions.

Plasma leptin, TG and FFA measurement. Blood was collected in EDTA microtubes from the tail vein of mice before and after 16 h of starvation. Plasma was obtained after 20 min of centrifugation at 1200 g at 4 °C. Leptin was measured with Mouse Leptin ELISA Kit following manufacturer's instructions after 6 h starvation. TGs were measured by a chemistry panel following standard protocols. FFA were measured using FFA assay HR-NEFA kit following manufacturer's instructions.

Ex vivo eWAT explants. Fresh eWAT depots were collected in ice-cold DMEM 1 g l^{-1} glucose + 0.5% FFA-free BSA, cut into small pieces and explants of ~25 mg of tissue and were placed in 24-well plates (one piece per well) with 500 µl of DMEM 1 g l^{-1} glucose + 0.5% FFA-free BSA. Baseline medium samples were obtained after 1 min of incubating the tissue at 37 °C with gentle shaking. Then, spermidine (50 µM) or equal volume of DMEM 1 g l^{-1} glucose + 0.5% FFA-free BSA was added. CL316243 was used as a positive control in all assays. Plates were incubated at 37 °C while shaking and aliquots of media (15 µl) were taken at 30, 60, 90 and 120 min. Alternatively, explants were incubated with 500 µl of conditioned medium and aliquots of medium were collected at baseline and 90 min. FFA concentration was quantified using an FFA assay HR-NEFA kit following manufacturer's instructions. When stated explants were preincubated 10 min with 100 µM propranolol at 37 °C before adding spermidine.

Targeted metabolomics. For metabolomic flux analysis ECs were incubated 2 and 4 h with DMEM high glucose, no glutamine, no methionine, no cystine plus [U-13C5]l-methionine 30 µg ml^{-1}, washed with PBS and snap-frozen in liquid nitrogen. For in vivo metabolomic flux analysis, [U-13C5]l-methionine was injected through the tail vein at 100 mg kg^{-1}; mice were killed 20 h after injection and adipose tissue was collected and snap-frozen in liquid nitrogen. For targeted metabolomic of conditioned medium, ECs were incubated 4 h in DMEM 1 g l^{-1} glucose + 0.5% FFA-free BSA, medium was collected and kept at −80 °C; protein content was used to normalize data (the experiment was performed with technical triplicates of six biological replicates for each genotype). To measure spermidine uptake, primary adipocytes were incubated with $^{13}C_4$ spermidine in DMEM 1 g l^{-1} glucose + 0.5% FFA-free BSA, washed with PBS and snap-frozen in liquid nitrogen; samples were taken at 0, 15, 30 and 60 min. For ex vivo metabolomic analysis adipose tissue was collected and immediately snap-frozen in liquid nitrogen. Levels of dcSAM and spermidine in WAT and adipose-derived ECs were analyzed by UPLC–MS, as previously described[46]. Briefly, extraction and homogenization were conducted in methanol/acetic acid (80/20% v/v). Speed-vacuum-dried metabolites were solubilized in 100 µl of a mixture of water/acetonitrile (40/60% v/v) and injected onto the UPLC–MS system (Acquity and SYNAPT G2, Waters). The extracted ion traces were obtained for dcSAM, spermine and spermidine. Corrected signals were normalized to protein content or mg of tissue.

Epinephrine and norepinephrine measure in WAT. WAT was homogenized in 500 µl of ice-cold extraction liquid and the aqueous phase was transferred to a fresh aliquot and placed at −80 °C for 20 min. The chilled supernatants were evaporated with a speedvac in approximately 2 h. The resulting pellets were resuspended in 150 µl water/acetonitrile (MeCN)/formic acid (40/60/0.1 v/v/%). Samples were measured with a UPLC system (Acquity, Waters) coupled to a time-of-flight mass spectrometer (ToF MS, SYNAPT G2, Waters). Extracted ion traces were obtained for the epinephrine fragment (m/z = 166.0859) and for norepinephrine fragment (m/z = 152.0731), in a 20-mDa window and subsequently smoothed and integrated with TargetLynx software (Waters). These calculated raw signals were adjusted for by median fold-change adjustment.

Statistics and reproducibility. Data were analyzed using GraphPad Prism 8.0.1 (GraphPad Software). Sample size and experimental replicates are indicated in figure legends. *P* values are included in the figures and the statistical test used is indicated in each figure legend. Mice and samples received a correlative number independent of their genotype, ensuring the blindness of data collection and analysis. Although no statistical methods were used to predetermine sample size, we aimed to have experimental groups of at least seven mice for all in vivo experiments. This group sampling was based on our expertise (minimum number of mice to provide robust and reliable data) and was feasible to obtain within our animal resources. In brackets is shown how many times each experiments was repeated independently with similar results for the indicated figures: Fig. 1c ($n=2$), Fig. 1f ($n=2$), Fig. 1i ($n=2$), Fig. 1j ($n=1$), Fig. 2a ($n=3$), Fig. 2c ($n=3$), Fig. 2e ($n=1$), Fig. 2g ($n=1$), Fig. 3b ($n=4$), Fig. 3e (eWAT $n=1$, iWAT $n=2$), Fig. 3i ($n=1$), Fig. 3l ($n=1$), Fig. 4e ($n=1$), Fig. 5i ($n=1$), Fig. 7i ($n=2$), Fig. 8a ($n=2$), Fig. 8j (n = 1), Extended Data Fig. 1b ($n=1$), Extended Data Fig. 1d ($n=3$), Extended Data Fig. 1e ($n=2$), Extended Data Fig. 1f ($n=1$), Extended Data Fig. 1g ($n=1$), Extended Data Fig. 2f ($n=3$), Extended Data Fig. 2i ($n=1$), Extended Data Fig. 2j ($n=1$), Extended Data Fig. 3a ($n=2$), Extended Data Fig. 3e ($n=1$), Extended Data Fig. 3f ($n=1$), Extended Data Fig. 4b ($n=2$), Extended Data Fig. 4g ($n=1$), Extended Data Fig. 4j ($n=1$), Extended Data Fig. 4o ($n=1$), Extended Data Fig. 5a ($n=1$), Extended Data Fig. 5d ($n=1$), Extended Data Fig. 6e ($n=1$), Extended Data Fig. 6k ($n=1$), Extended Data Fig. 7k ($n=1$) and Extended Data Fig. 10l ($n=1$).

Reporting Summary. Further information on research design is available in the Nature Research Reporting Summary linked to this article.

Data availability

Image source data and Excel files of all data presented in graphs within the figures and extended data figures have been supplied in Source Data files. Separate files for each figure have been supplied.

Received: 15 September 2021; Accepted: 2 February 2022;
Published online: 14 March 2022

References

1. Kruger-Genge, A., Blocki, A., Franke, R. P. & Jung, F. Vascular endothelial cell biology: an update. *Int. J. Mol. Sci.* https://doi.org/10.3390/ijms20184411 (2019).
2. Graupera, M. & Claret, M. Endothelial cells: new players in obesity and related metabolic disorders. *Trends Endocrinol. Metab.* **29**, 781–794 (2018).
3. Hasan, S. S. & Fischer, A. The endothelium: an active regulator of lipid and glucose homeostasis. *Trends Cell Biol.* **31**, 37–49 (2021).
4. Arany, Z. et al. HIF-independent regulation of VEGF and angiogenesis by the transcriptional coactivator PGC-1α. *Nature* **451**, 1008–1012 (2008).
5. Fan, Z. et al. Exercise-induced angiogenesis is dependent on metabolically primed ATF3/4(+) endothelial cells. *Cell Metab.* **33**, 1793–1807 (2021).
6. Potente, M., Gerhardt, H. & Carmeliet, P. Basic and therapeutic aspects of angiogenesis. *Cell* **146**, 873–887 (2011).
7. Eelen, G., Treps, L., Li, X. & Carmeliet, P. Basic and therapeutic aspects of angiogenesis updated. *Circ. Res* **127**, 310–329 (2020).
8. Kobialka, P. & Graupera, M. Revisiting PI3-kinase signalling in angiogenesis. *Vasc. Biol.* **1**, H125–H134 (2019).
9. Bilanges, B., Posor, Y. & Vanhaesebroeck, B. PI3K isoforms in cell signalling and vesicle trafficking. *Nat. Rev. Mol. Cell Biol.* **20**, 515–534 (2019).
10. Song, M. S., Salmena, L. & Pandolfi, P. P. The functions and regulation of the PTEN tumour suppressor. *Nat. Rev. Mol. Cell Biol.* **13**, 283–296 (2012).
11. Angulo-Urarte, A. et al. Endothelial cell rearrangements during vascular patterning require PI3-kinase-mediated inhibition of actomyosin contractility. *Nat. Commun.* **9**, 4826 (2018).
12. Hare, L. M. et al. Heterozygous expression of the oncogenic Pik3ca(H1047R) mutation during murine development results in fatal embryonic and extraembryonic defects. *Dev. Biol.* **404**, 14–26 (2015).
13. Kobialka, P. S. H. et al. Low dose AKT inhibitor miransertib cures PI3K-related vascular malformations in preclinical models of human disease. Preprint at *bioRxiv* https://doi.org/10.1101/2021.07.16.452617 (2021).
14. Serra, H. et al. PTEN mediates Notch-dependent stalk cell arrest in angiogenesis. *Nat. Commun.* **6**, 7935 (2015).
15. Lesche, R. et al. Cre/loxP-mediated inactivation of the murine Pten tumor suppressor gene. *Genesis* **32**, 148–149 (2002).
16. Claxton, S. et al. Efficient, inducible Cre-recombinase activation in vascular endothelium. *Genesis* **46**, 74–80 (2008).
17. Sanz, E. et al. Cell-type-specific isolation of ribosome-associated mRNA from complex tissues. *Proc. Natl Acad. Sci. USA* **106**, 13939–13944 (2009).
18. Wang, Y. et al. Ephrin-B2 controls VEGF-induced angiogenesis and lymphangiogenesis. *Nature* **465**, 483–486 (2010).
19. Rupnick, M. A. et al. Adipose tissue mass can be regulated through the vasculature. *Proc. Natl Acad. Sci. USA* **99**, 10730–10735 (2002).
20. Cao, Y. Angiogenesis and vascular functions in modulation of obesity, adipose metabolism, and insulin sensitivity. *Cell Metab.* **18**, 478–489 (2013).

21. Herold, J. & Kalucka, J. Angiogenesis in adipose tissue: the interplay between adipose and endothelial cells. *Front. Physiol.* **11**, 624903 (2020).
22. Robciuc, M. R. et al. VEGFB/VEGFR1-induced expansion of adipose vasculature counteracts obesity and related metabolic complications. *Cell Metab.* **23**, 712–724 (2016).
23. Sung, H. K. et al. Adipose vascular endothelial growth factor regulates metabolic homeostasis through angiogenesis. *Cell Metab.* **17**, 61–72 (2013).
24. Elias, I. et al. Adipose tissue overexpression of vascular endothelial growth factor protects against diet-induced obesity and insulin resistance. *Diabetes* **61**, 1801–1813 (2012).
25. Rudnicki, M. et al. Endothelial-specific FoxO1 depletion prevents obesity-related disorders by increasing vascular metabolism and growth. *eLife* https://doi.org/10.7554/eLife.39780 (2018).
26. Sun, K. et al. Dichotomous effects of VEGF-A on adipose tissue dysfunction. *Proc. Natl Acad. Sci. USA* **109**, 5874–5879 (2012).
27. Carracedo, A. et al. A metabolic prosurvival role for PML in breast cancer. *J. Clin. Invest* **122**, 3088–3100 (2012).
28. Enguix, N. et al. Mice lacking PGC-1β in adipose tissues reveal a dissociation between mitochondrial dysfunction and insulin resistance. *Mol. Metab.* **2**, 215–226 (2013).
29. Collins, S. & Surwit, R. S. The β-adrenergic receptors and the control of adipose tissue metabolism and thermogenesis. *Recent Prog. Horm. Res* **56**, 309–328 (2001).
30. Lee, M. J., Wu, Y. & Fried, S. K. Adipose tissue heterogeneity: implication of depot differences in adipose tissue for obesity complications. *Mol. Asp. Med.* **34**, 1–11 (2013).
31. Rosen, E. D. & Spiegelman, B. M. What we talk about when we talk about fat. *Cell* **156**, 20–44 (2014).
32. Rafii, S., Butler, J. M. & Ding, B. S. Angiocrine functions of organ-specific endothelial cells. *Nature* **529**, 316–325 (2016).
33. Augustin, H. G. & Koh, G. Y. Organotypic vasculature: from descriptive heterogeneity to functional pathophysiology. *Science* https://doi.org/10.1126/science.aal2379 (2017).
34. Cleaver, O. & Melton, D. A. Endothelial signaling during development. *Nat. Med.* **9**, 661–668 (2003).
35. Zhang, J. et al. Endothelial lactate controls muscle regeneration from ischemia by inducing m2-like macrophage polarization. *Cell Metab.* **31**, 1136–1153 (2020).
36. Crewe, C. et al. An endothelial-to-adipocyte extracellular vesicle axis governed by metabolic state. *Cell* **175**, 695–708 (2018).
37. Casero, R. A. Jr., Murray Stewart, T. & Pegg, A. E. Polyamine metabolism and cancer: treatments, challenges and opportunities. *Nat. Rev. Cancer* **18**, 681–695 (2018).
38. Arruabarrena-Aristorena, A., Zabala-Letona, A. & Carracedo, A. Oil for the cancer engine: the cross-talk between oncogenic signaling and polyamine metabolism. *Sci. Adv.* **4**, eaar2606 (2018).
39. Pegg, A. E. Functions of polyamines in mammals. *J. Biol. Chem.* **291**, 14904–14912 (2016).
40. Kraus, D. et al. Nicotinamide N-methyltransferase knockdown protects against diet-induced obesity. *Nature* **508**, 258–262 (2014).
41. Ramos-Molina, B., Queipo-Ortuno, M. I., Lambertos, A., Tinahones, F. J. & Penafiel, R. Dietary and gut microbiota polyamines in obesity- and age-related diseases. *Front Nutr.* **6**, 24 (2019).
42. Pirinen, E. et al. Enhanced polyamine catabolism alters homeostatic control of white adipose tissue mass, energy expenditure, and glucose metabolism. *Mol. Cell Biol.* **27**, 4953–4967 (2007).
43. Sadasivan, S. K. et al. Exogenous administration of spermine improves glucose utilization and decreases bodyweight in mice. *Eur. J. Pharm.* **729**, 94–99 (2014).
44. Gao, M. et al. Spermidine ameliorates non-alcoholic fatty liver disease through regulating lipid metabolism via AMPK. *Biochem. Biophys. Res. Commun.* **505**, 93–98 (2018).
45. Rajeeve, V., Pearce, W., Cascante, M., Vanhaesebroeck, B. & Cutillas, P. R. Polyamine production is downstream and upstream of oncogenic PI3K signalling and contributes to tumour cell growth. *Biochem. J.* **450**, 619–628 (2013).
46. Zabala-Letona, A. et al. mTORC1-dependent AMD1 regulation sustains polyamine metabolism in prostate cancer. *Nature* **547**, 109–113 (2017).
47. Meana, C. et al. Functional effects of polyamines via activation of human β1- and β2-adrenoceptors stably expressed in CHO cells. *Pharm. Rep.* **62**, 696–706 (2010).
48. Gomez-Salinero, J. M., Itkin, T. & Rafii, S. Developmental angiocrine diversification of endothelial cells for organotypic regeneration. *Dev. Cell* **56**, 3042–3051 (2021).
49. Ding, B. S. et al. Endothelial-derived angiocrine signals induce and sustain regenerative lung alveolarization. *Cell* **147**, 539–553 (2011).
50. Ding, B. S. et al. Divergent angiocrine signals from vascular niche balance liver regeneration and fibrosis. *Nature* **505**, 97–102 (2014).
51. Cao, Z. et al. Angiocrine factors deployed by tumor vascular niche induce B cell lymphoma invasiveness and chemoresistance. *Cancer Cell* **25**, 350–365 (2014).
52. Ottone, C. et al. Direct cell–cell contact with the vascular niche maintains quiescent neural stem cells. *Nat. Cell Biol.* **16**, 1045–1056 (2014).
53. Lorenz, L. et al. Mechanosensing by β1 integrin induces angiocrine signals for liver growth and survival. *Nature* **562**, 128–132 (2018).
54. Singhal, M. et al. Temporal multi-omics identifies LRG1 as a vascular niche instructor of metastasis. *Sci. Transl. Med.* **13**, eabe6805 (2021).
55. Liu, Z. et al. Glycolysis links reciprocal activation of myeloid cells and endothelial cells in the retinal angiogenic niche. *Sci. Transl. Med.* https://doi.org/10.1126/scitranslmed.aay1371 (2020).
56. De Bock, K. et al. Role of PFKFB3-driven glycolysis in vessel sprouting. *Cell* **154**, 651–663 (2013).
57. Schoors, S. et al. Fatty acid carbon is essential for dNTP synthesis in endothelial cells. *Nature* **520**, 192–197 (2015).
58. Wong, B. W. et al. The role of fatty acid β-oxidation in lymphangiogenesis. *Nature* **542**, 49–54 (2017).
59. Chen, J. et al. High-resolution 3D imaging uncovers organ-specific vascular control of tissue aging. *Sci. Adv.* https://doi.org/10.1126/sciadv.abd7819 (2021).
60. Grunewald, M. et al. Counteracting age-related VEGF signaling insufficiency promotes healthy aging and extends life span. *Science* https://doi.org/10.1126/science.abc8479 (2021).
61. Bordallo, C. et al. Putrescine modulation of acute activation of the β-adrenergic system in the left atrium of rat. *Eur. J. Pharm.* **598**, 68–74 (2008).
62. Sanchez, M. et al. Role of beta-adrenoceptors, cAMP phosphodiesterase and external Ca^{2+} on polyamine-induced relaxation in isolated bovine tracheal strips. *Pharm. Rep.* **62**, 1127–1138 (2010).
63. Ma, L. et al. Spermidine ameliorates high-fat diet-induced hepatic steatosis and adipose tissue inflammation in preexisting obese mice. *Life Sci.* **265**, 118739 (2021).
64. Zhang, L., Gong, H., Sun, Q., Zhao, R. & Jia, Y. Spermidine-activated satellite cells are associated with hypoacetylation in ACVR2B and Smad3 binding to myogenic genes in mice. *J. Agric Food Chem.* **66**, 540–550 (2018).
65. Eilken, H. M. et al. Pericytes regulate VEGF-induced endothelial sprouting through VEGFR1. *Nat. Commun.* **8**, 1574 (2017).
66. Czyzyk, T. A. et al. κ-Opioid receptors control the metabolic response to a high-energy diet in mice. *FASEB J.* **24**, 1151–1159 (2010).
67. Nogueiras, R. et al. Direct control of peripheral lipid deposition by CNS GLP-1 receptor signaling is mediated by the sympathetic nervous system and blunted in diet-induced obesity. *J. Neurosci.* **29**, 5916–5925 (2009).
68. Czyzyk, T. A. et al. Mice lacking delta-opioid receptors resist the development of diet-induced obesity. *FASEB J.* **26**, 3483–3492 (2012).
69. Canto, C. & Garcia-Roves, P. M. High-resolution respirometry for mitochondrial characterization of ex vivo mouse tissues. *Curr. Protoc. Mouse Biol.* **5**, 135–153 (2015).
70. Deberardinis, R. J., Lum, J. J. & Thompson, C. B. Phosphatidylinositol 3-kinase-dependent modulation of carnitine palmitoyltransferase 1A expression regulates lipid metabolism during hematopoietic cell growth. *J. Biol. Chem.* **281**, 37372–37380 (2006).

Acknowledgements

We thank members of the Endothelial Pathobiology and Microenvironment Group for helpful discussions. We thank the CERCA Program/Generalitat de Catalunya and the Josep Carreras Foundation for institutional support. The research leading to these results has received funding from la Fundación BBVA (Ayuda Fundacion BBVA a Equipos de Investigación Científica 2019, PR19BIOMET0061) and from SAF2017-82072-ERC from Ministerio de Ciencia, Innovación y Universidades (MCIU) (Spain). The laboratory of M.G. is also supported by the research grants SAF2017-89116R-P (FEDER/EU) co-funded by European Regional Developmental Fund (ERDF), a Way to Build Europe and PID2020-116184RB-I00 from MCEI; by the Catalan Government through the project 2017-SGR; PTEN Research Foundation (BRR-17-001); La Caixa Foundation (HR19-00120 and HR21-00046); by la Asociación Española contra el Cancer-Grupos Traslacionales (GCTRA18006CARR, also to A.C.); European Foundation for the Study of Diabetes/Lilly research grant, also to M.C.); and by the People Programme (Marie Curie Actions; grant agreement 317250) of the European Union's Seventh Framework Programme FP7/2007-2013 and the Marie Skłodowska-Curie (grant agreement 675392) of the European Union's Horizon 2020 research. The laboratory of A.C. is supported by the Basque Department of Industry, Tourism and Trade (Elkartek) and the department of education (IKERTALDE IT1106-16), the MCIU (PID2019-108787RB-I00 (FEDER/EU); Severo Ochoa Excellence Accreditation SEV-2016-0644; Excellence Networks SAF2016-81975-REDT), La Caixa Foundation (ID 100010434), under the agreement LCF/PR/HR17, the Vencer el Cancer foundation and the European Research Council (ERC) (consolidator grant 819242). CIBERONC was co-funded with FEDER funds and funded by Instituto de Salud Carlos III (ISCIII). The laboratory of M.C. is supported by the ERC under the European Union's Horizon 2020 research and innovation programme (grant agreement 725004) and CERCA Programme/Generalitat de Catalunya (M.C.).

The laboratory of D.S. is supported by research grants from MINECO (SAF2017-83813-C3-1-R, also to L.H., cofounded by the ERDF), CIBEROBN (CB06/03/0001), Government of Catalonia (2017SGR278) and Fundació La Marató de TV3 (201627-30). The laboratory of R.N. is supported by FEDER/Ministerio de Ciencia, Innovación y Universidades-Agencia Estatal de Investigación (RTI2018-099413-B-I00 and and RED2018-102379-T), Xunta de Galicia (2016-PG057 and 2020-PG015), ERC under the European Union's Horizon 2020 research and innovation programme (grant agreement 810331), Fundación BBVA, Fundacion Atresmedia and CIBEROBN, which is an initiative of the ISCIII of Spain, which is supported by FEDER funds. The laboratory of J.A.V. is supported by research grants from MICINN (RTI2018-099250-B100) and by La Caixa Foundation (ID 100010434, LCF/PR/HR17/52150009). P.M.G.-R. is supported by ISCIII grant PI15/00701 cofinanced by the ERDF, A Way to Build Europe. Personal support was from Marie Curie ITN Actions (E.M.), Juan de la Cierva (IJCI-2015-23455, P.V.), CONICYT fellowship from Chile (S.Z.), Vetenskapsradet (Swedish Research Council, 2018-06591, L.G.) and NCI K99/R00 Pathway to Independence Award (K99CA245122, P. Castel).

Author contributions

E.M., M.C., A.C. and M.G. conceived the project. E.M., P.V., L.G., A.Z.-L., A.M.-R., J.L.L., D.B., L.G., I.C., S.Z., P.G.-P. O.O.-C., L.M., A.M.-G., S.D.C., N.M.-M, P. Castel, L.V.-J., I.G.-G. and S.F.-R. performed experiments and analyzed data with the supervision of J.V., D.S., L.H., R.B., P.G.-R., R.N., P. Cohen, M.C., A.C. and M.G. E.M., P.V., L.G., S.D.C., A.C. and M.G. wrote the manuscript and designed the Figures. L.H., D.B., R.N., P.G.-R., M.C., A.C. and M.G. provided funding.

Competing interests

M.G. has a research agreement with Merck and Venthera. None of those have a relationship with adipose tissue vasculature. The remaining authors declare no competing interests.

Additional information

Extended data is available for this paper at https://doi.org/10.1038/s42255-022-00544-6.

Supplementary information The online version contains supplementary material available at https://doi.org/10.1038/s42255-022-00544-6.

Correspondence and requests for materials should be addressed to Mariona Graupera.

Peer review information *Nature Metabolism* thanks the anonymous reviewers for their contribution to the peer review of this work. Primary handling editor: Christoph Schmitt.

Reprints and permissions information is available at www.nature.com/reprints.

Publisher's note Springer Nature remains neutral with regard to jurisdictional claims in published maps and institutional affiliations.

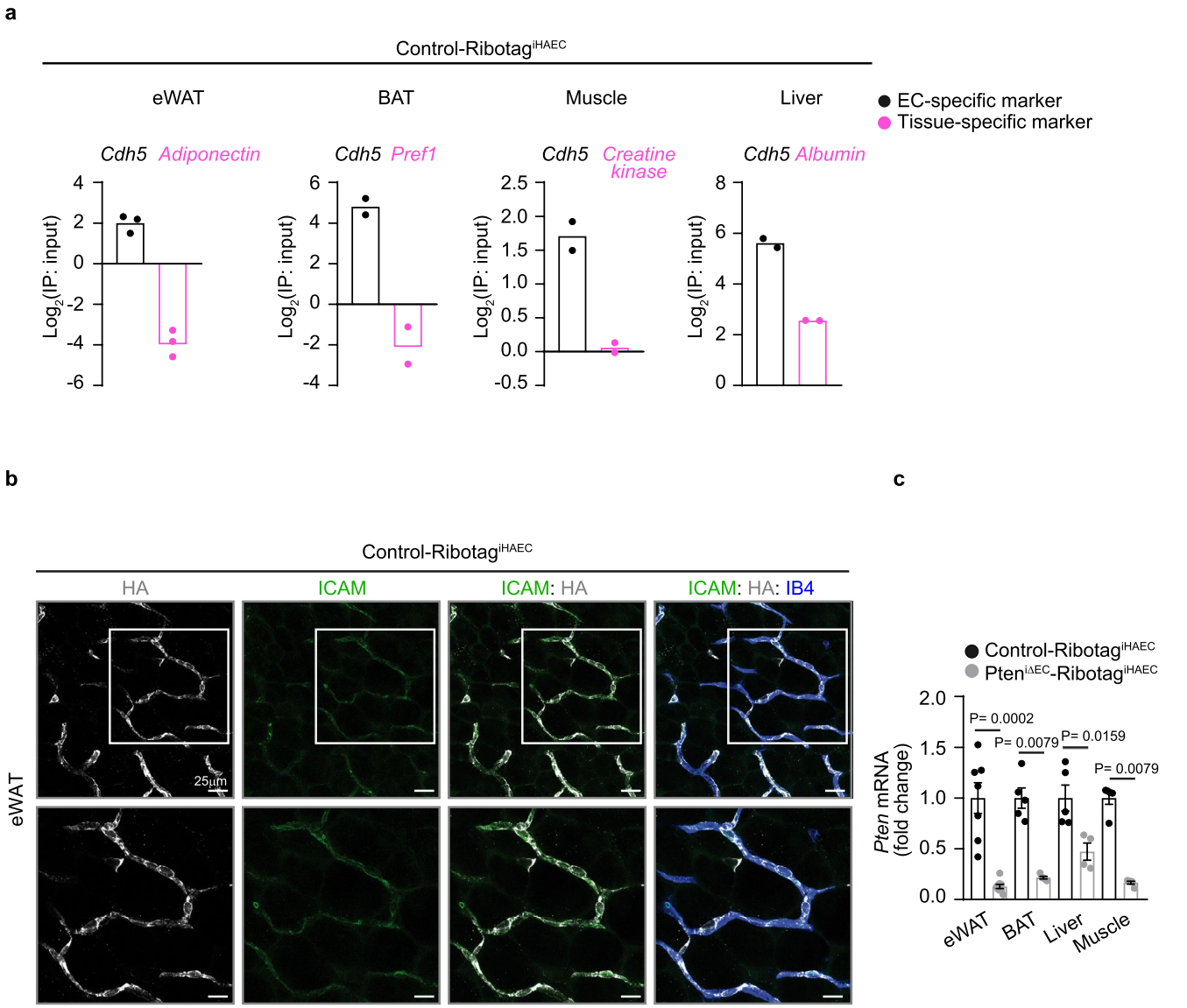

Extended Data Fig. 1 | See next page for caption.

Extended Data Fig. 1 | Validation of *Pten* deletion in *Pten*$^{i\Delta EC}$ mice. a) Enrichment ratios of expression of VE-cadherin (*Cdh5*) and tissue-specific gene in endothelial cell-specific mRNA preparations from eWAT, BAT, muscle and liver after ribosome immunoprecipitation from *Ribotag*^{iHAEC} mice (eWAT n = 3, BAT, muscle and liver n = 2). (**b**) Representative images of flat-mounted eWAT from 5-week-old control *Ribotag*^{iHAEC} mice stained with HA (white), ICAM2 (green) and isolectin (IB4) (blue). White islets show high magnification of selected regions shown below. (**c**) Quantification of *Pten* mRNA levels in WAT, BAT liver and muscle endothelium from *Ribotag*^{iHAEC} and *Pten*$^{i\Delta EC}$- *Ribotag*^{iHAEC} at 5 weeks of age (n = 6 per group). (**d**-**g**) Western blot analysis of Pten expression in (**d**) adipose-EC obtained from control (n = 5) and *Pten*$^{i\Delta EC}$ mice (n = 6), (**e**) lung-EC obtained from control (n = 6) and *Pten*$^{i\Delta EC}$ mice (n = 6), (**f**) muscle-EC obtained from control (n = 4) and *Pten*$^{i\Delta EC}$ mice (n = 5) and (**g**) BAT-EC obtained from control (n = 3) and *Pten*$^{i\Delta EC}$ mice (n = 6). Data represent mean ± SEM (error bars). Samples represent biological replicates. Statistical analysis was performed by the two-sided Mann-Whitney test (Extended Data Fig. 1c).

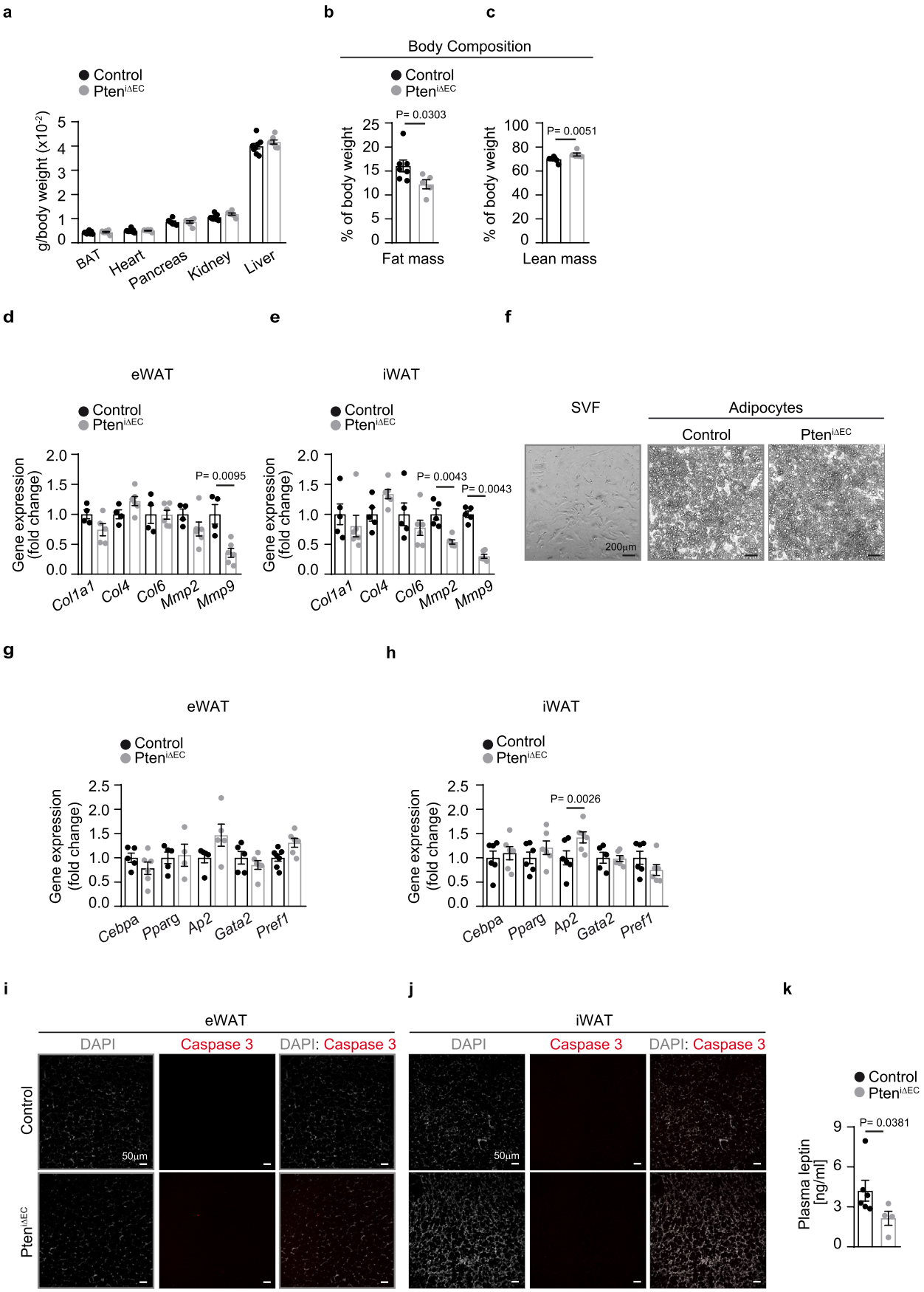

Extended Data Fig. 2 | See next page for caption.

Extended Data Fig. 2 | Endothelial *Pten* loss leads to reduced fat mass, and it is not associated with fibrosis, altered differentiation or cell death. (a) Tissue weight in control and $Pten^{i\Delta EC}$ mice at 12 weeks of age (control n = 8, $Pten^{i\Delta EC}$ n = 6). (b and c) Body composition analysis of control and $Pten^{i\Delta EC}$ mice at 14 weeks (control n = 7, $Pten^{i\Delta EC}$ n = 5) by MRI. (d and e) Gene expression analysis of fibrosis markers in whole tissue extracts from (d) eWAT (control n = 4, $Pten^{i\Delta EC}$ n = 6) and (e) iWAT (control n = 5, $Pten^{i\Delta EC}$ n = 6) from control and $Pten^{i\Delta EC}$ mice at 12 weeks of age. (f) Representative microscopic images showing *in vitro* adipocyte differentiation from preadipocytes (contained in the stromal vascular fraction (SVF) obtained from iWAT depots from 6-week-old control and $Pten^{i\Delta EC}$ mice. A representative image of cultured SVF prior to differentiation is shown to the left. (g and h) Gene expression analysis of adipocyte differentiation markers in whole tissue extracts from (g) eWAT (control n = 5, $Pten^{i\Delta EC}$ n = 4) and (h) iWAT (control n = 4, $Pten^{i\Delta EC}$ n = 5) from control and $Pten^{i\Delta EC}$ mice at 12 weeks of age. (i and j) Representative confocal images of (i) eWAT and (j) iWAT sections stained with cleaved caspase-3 (red) and DAPI (white) from 12-week-old control and $Pten^{i\Delta EC}$ mice. (k) Levels of leptin in serum of control and $Pten^{i\Delta EC}$ mice at 14 weeks of age (control n = 5, $Pten^{i\Delta EC}$ n = 4). Data represent mean ± SEM (error bars). Samples represent biological replicates. Statistical analysis was performed by the two-sided Mann-Whitney test (Extended Data Fig. 2b, c, d, e, g, k).

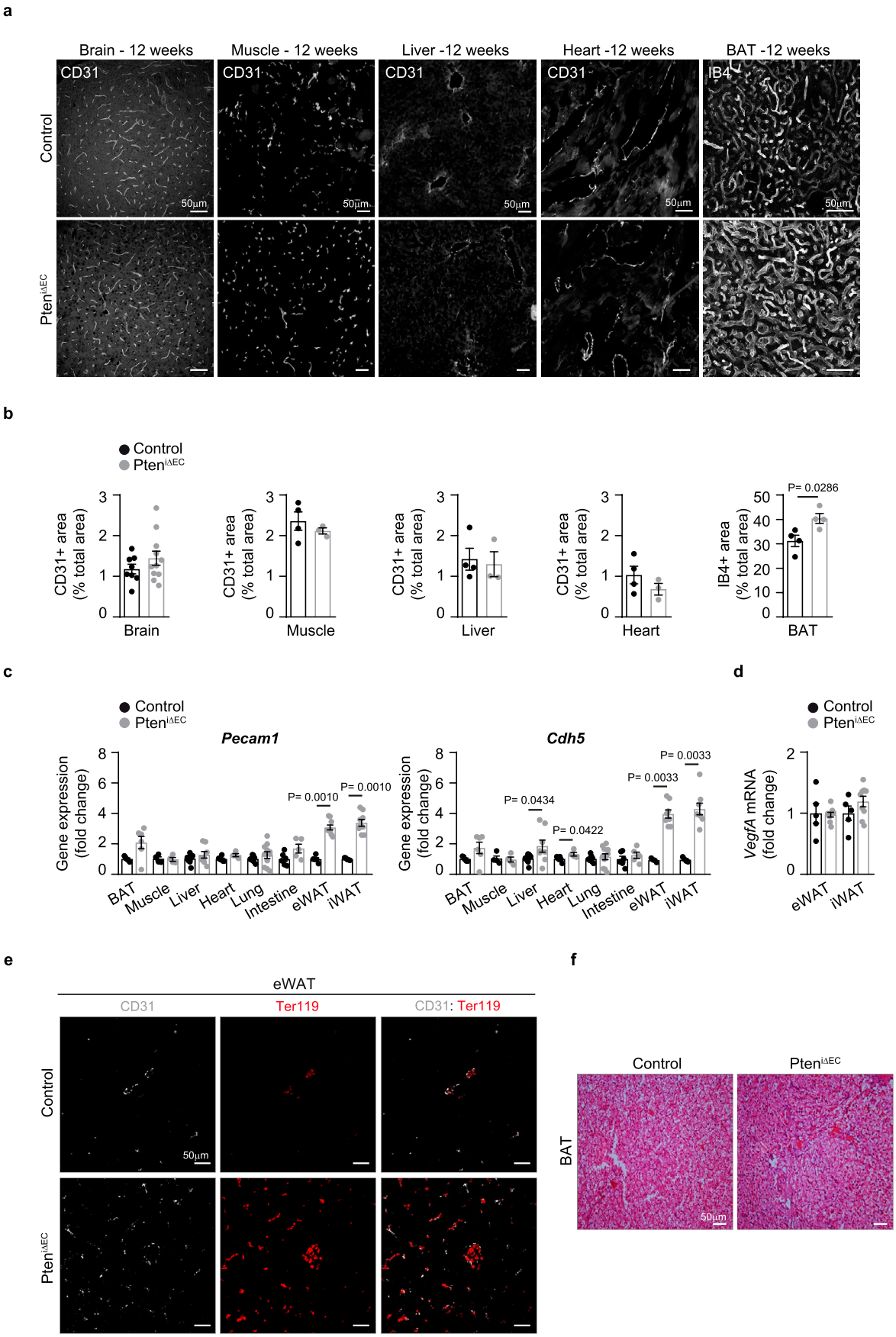

Extended Data Fig. 3 | See next page for caption.

Extended Data Fig. 3 | Molecular and histological vascular characterization in several tissues of control and *Pten*$^{i\Delta EC}$ mice. (a) Representative images of CD31-stained blood vessels (white) in sections from brain, muscle, liver and heart and IB4-stained blood vessels (white) in cryosections of BAT and from control (upper panels) and *Pten*$^{i\Delta EC}$ mice (lower panels) at 12 weeks of age. (b) Quantification of vessel density expressed as percentage of total area in brain, muscle, liver, heart, and BAT sections from control and *Pten*$^{i\Delta EC}$ mice at 12 weeks of age (brain n = 8, muscle, liver and heart control n = 4, *Pten*$^{i\Delta EC}$ n = 3, BAT n = 4). (c) Gene expression analysis of endothelial markers *Pecam1* (left graph) and *Cdh5* (right graph) in whole tissue extracts from control and *Pten*$^{i\Delta EC}$ mice at 5 weeks of age (BAT n = 5, muscle n = 4, liver n = 8, heart n = 4, lung n = 9, intestine n = 5, eWAT=5, iWAT=5). (d) *VegfA* gene expression analysis in whole tissue extracts from eWAT and iWAT from control (n = 5) and *Pten*$^{i\Delta EC}$ (n = 9) mice at 12 weeks of age. (e) Representative images of CD31 (white) and Ter119 (red) stained sections of control and *Pten*$^{i\Delta EC}$ eWAT at 12 weeks of age. (h) Representative hematoxylin and eosin staining of BAT sections from control and *Pten*$^{i\Delta EC}$ mice at 12 weeks of age. Data represent mean ± SEM (error bars). Samples represent biological replicates. Statistical analysis was performed by the two-sided Mann-Whitney test (Extended Data Fig. 3b, c, d).

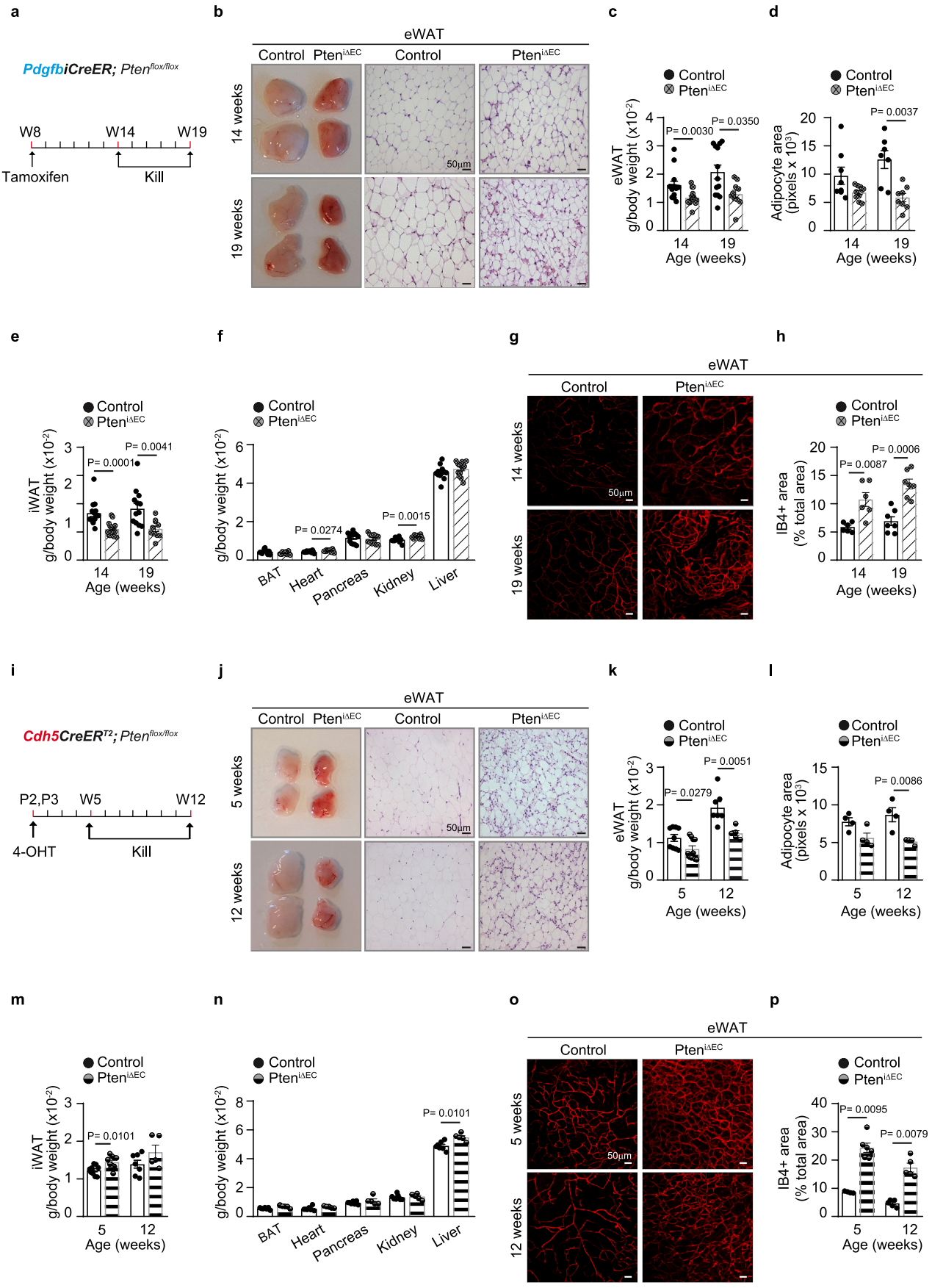

Extended Data Fig. 4 | See next page for caption.

Extended Data Fig. 4 | *In vivo* characterization upon endothelial *Pten* loss. (**a,i**) Scheme illustrating the experimental protocol. (**b**) Representative images of eWAT from control and $Pten^{i\Delta EC}$ mice at 14 and 19 weeks of age. (**c**) eWAT pad weight at 14 (control n = 15, $Pten^{i\Delta EC}$ n = 16) and 19 (control n = 13, $Pten^{i\Delta EC}$ n = 10) weeks of age, (**d**) Quantification of adipocyte area of eWAT at 14 (control n = 8, $Pten^{i\Delta EC}$ n = 10) and 19 (control n = 7, $Pten^{i\Delta EC}$ n = 8) weeks of age, (**e**) iWAT pad weight at 14 (control n = 14, $Pten^{i\Delta EC}$ n = 16) and 19 (control n = 13, $Pten^{i\Delta EC}$ n = 10) weeks of age from control and $Pten^{i\Delta EC}$ mice. (**f**) Tissue weight in control and $Pten^{i\Delta EC}$ mice at 14 weeks of age (n = 11). (**g**) Confocal images of eWAT whole-mount staining with IB4 (red) from control and $Pten^{i\Delta EC}$ mice at 14 and 19 weeks of age. (**h**) Quantification of IB4-positive area in eWAT depots from control and $Pten^{i\Delta EC}$ mice at 14 (n = 6 per group) and 19 weeks of age (n = 7 per group). (**j**) Representative images of eWAT from control and $Pten^{i\Delta EC}$ mice at 5 and 12 weeks of age. (**k**) eWAT pad weight in control and $Pten^{i\Delta EC}$ mice at 5 (control n = 9, $Pten^{i\Delta EC}$ n = 10) and 12 (control n = 7, $Pten^{i\Delta EC}$ n = 5) weeks of age. (**l**) Quantification of adipocyte area of eWAT from control and $Pten^{i\Delta EC}$ mice at 5 (n = 4) and 12 (n = 4) weeks of age. (**m**) iWAT pad weight in control and $Pten^{i\Delta EC}$ mice at 5 (control n = 9, $Pten^{i\Delta EC}$ n = 10) and 12 (control n = 7, $Pten^{i\Delta EC}$ n = 5) weeks of age. (**n**) Tissue weight in control and $Pten^{i\Delta EC}$ mice at 12 weeks of age (control n = 7, $Pten^{i\Delta EC}$ n = 5). (**o**) Confocal images of eWAT whole-mount staining with IB4 (red) from control and $Pten^{i\Delta EC}$ mice at 5 and 12 weeks of age. (**p**) Quantification of IB4-positive area in eWAT depots from control and $Pten^{i\Delta EC}$ mice at 5 and 12 weeks of age (control n = 7, $Pten^{i\Delta EC}$ n = 5). Data represent mean ± SEM (error bars). Samples represent biological replicates. Statistical analysis was performed by the two-sided Mann-Whitney test (Extended Data Fig. 4c, d, e, f, h, k, l, m, n, p).

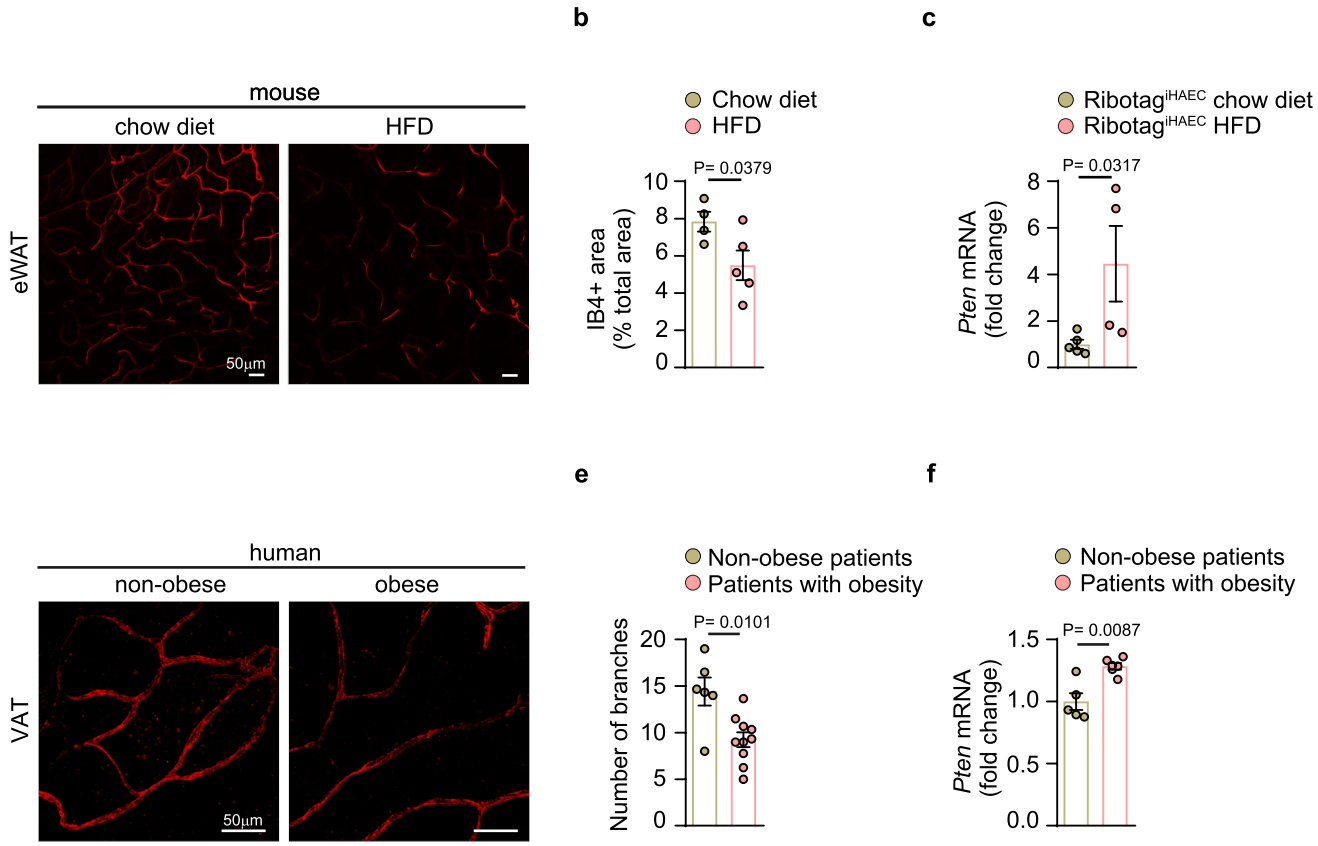

Extended Data Fig. 5 | Low endothelial *Pten* expression correlates with high vascular content in mouse and human white adipose tissue. (a) Representative confocal images of wild-type eWAT whole-mount staining with IB4 (red) after 12 weeks of chow diet or HFD. (**b**) Quantification of IB4 positive area in eWAT from wild-type mice exposed to chow diet or HFD for 12 weeks (chow diet n = 4, HFD n = 5). (**c**) *In vivo Pten* mRNA expression levels in adipose endothelial cells from wild-type *Ribotag*^{iHAEC} mice after exposure to chow diet or HFD for 12 weeks (chow diet n = 5, HFD n = 4). (**d**) Representative confocal images of visceral adipose tissue (VAT) whole-mount stained with CD31 (red) from non-obese and patients with obesity. (**e**) Quantification of vessel branches in VAT whole-mount stained with CD31 from non-obese and patients with obesity (non-obese n = 6, obese n = 10). (**f**) *Pten* mRNA expression levels in VAT tissue extracts from non-obese and patients with obesity (non-obese n = 5, obese n = 6). Data represent mean ± SEM (error bars). Samples represent biological replicates. Statistical analysis was performed by the two-sided Mann-Whitney test (Extended Data Fig. 5b, c, e, f).

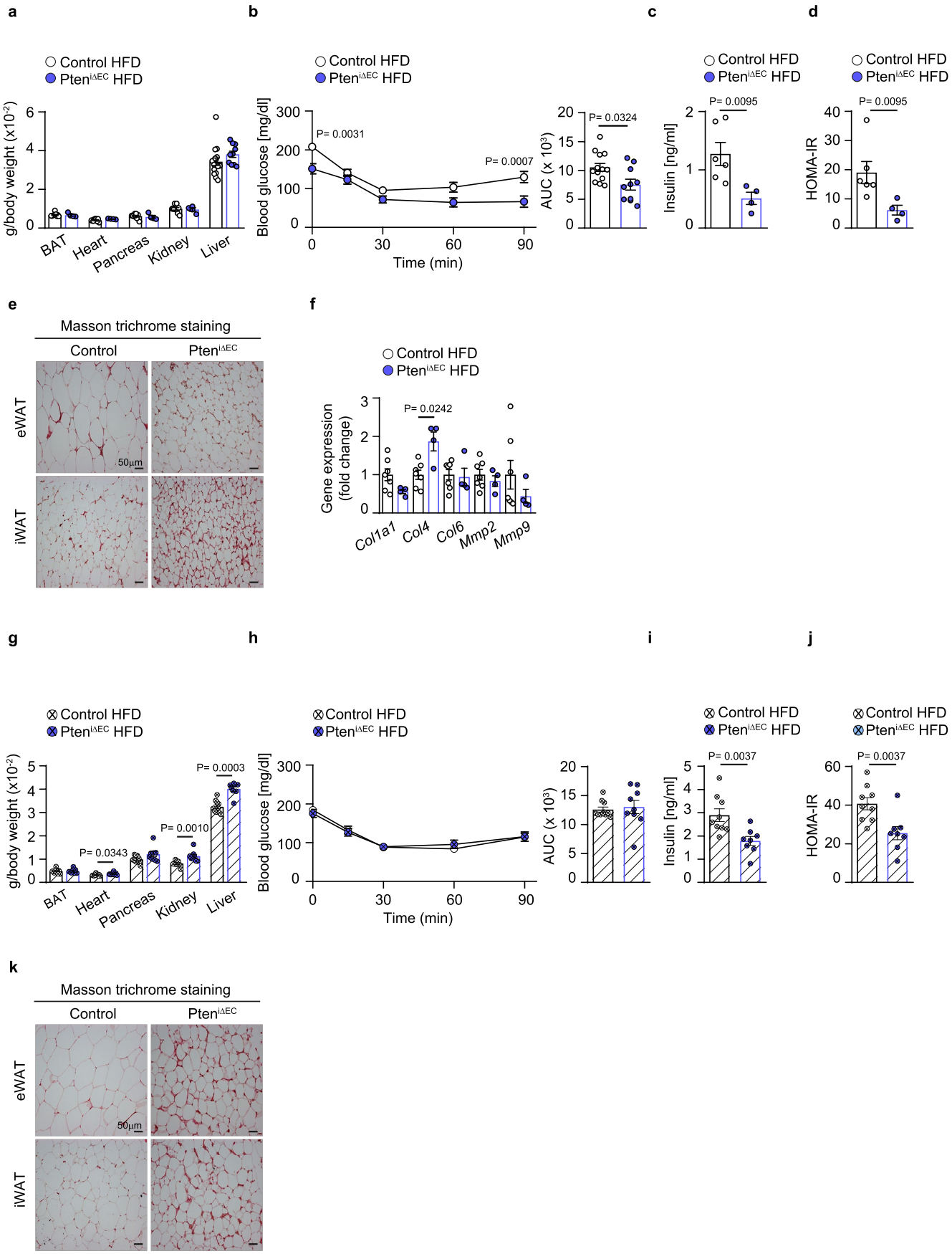

Extended Data Fig. 6 | See next page for caption.

Extended Data Fig. 6 | Low endothelial *Pten* expression correlates with improved glucose systemic metabolism in mice. (a) Tissue weight in control and *Pten*$^{i\Delta EC}$ mice exposed to HFD for 10 weeks (control n = 9, *Pten*$^{i\Delta EC}$ n = 4). (**b**) Insulin tolerance test (ITT) performed in control and *Pten*$^{i\Delta EC}$ mice fed with HFD for 10 weeks (control n = 13, *Pten*$^{i\Delta EC}$ n = 10). Bars to the right show AUC quantification of blood glucose monitoring during ITT (control n = 13, *Pten*$^{i\Delta EC}$ n = 10). (**c**) Basal insulin levels and (**d**) HOMA-IR index in control and *Pten*$^{i\Delta EC}$ mice fed with HFD for 10 weeks (control n = 6, *Pten*$^{i\Delta EC}$ n = 4). (**e**) Masson trichrome fibrosis staining in eWAT and iWAT sections from control and *Pten*$^{i\Delta EC}$ mice exposed to HFD for 10 weeks. (**f**) Gene expression analysis of fibrosis markers in whole tissue extracts from eWAT (control n = 7, *Pten*$^{i\Delta EC}$ n = 4) from control and *Pten*$^{i\Delta EC}$ mice exposed to HFD for 10 weeks. (**g**) Tissue weight in control and *Pten*$^{i\Delta EC}$ mice exposed to HFD for 34 weeks (control n = 9, *Pten*$^{i\Delta EC}$ n = 8). (**h**) ITT performed in control and *Pten*$^{i\Delta EC}$ mice fed with HFD for 30 weeks (control n = 10, *Pten*$^{i\Delta EC}$ n = 9). Bars to the right show AUC quantification of blood glucose monitoring during ITT. (**i**) Basal insulin levels and (**j**) HOMA-IR index in control and *Pten*$^{i\Delta EC}$ mice fed with HFD for 34 weeks (control n = 9, *Pten*$^{i\Delta EC}$ n = 8). (**k**) Masson trichrome fibrosis staining in eWAT and iWAT sections from control and *Pten*$^{i\Delta EC}$ mice exposed to HFD for 34 weeks. Data represent mean ± SEM (error bars). Samples represent biological replicates. Statistical analysis was performed by the two-sided Mann-Whitney test (Extended Data Fig. 6a, c, d, f, i, j) and 2-way ANOVA with Bonferroni correction (Extended Data Fig. 6b, h).

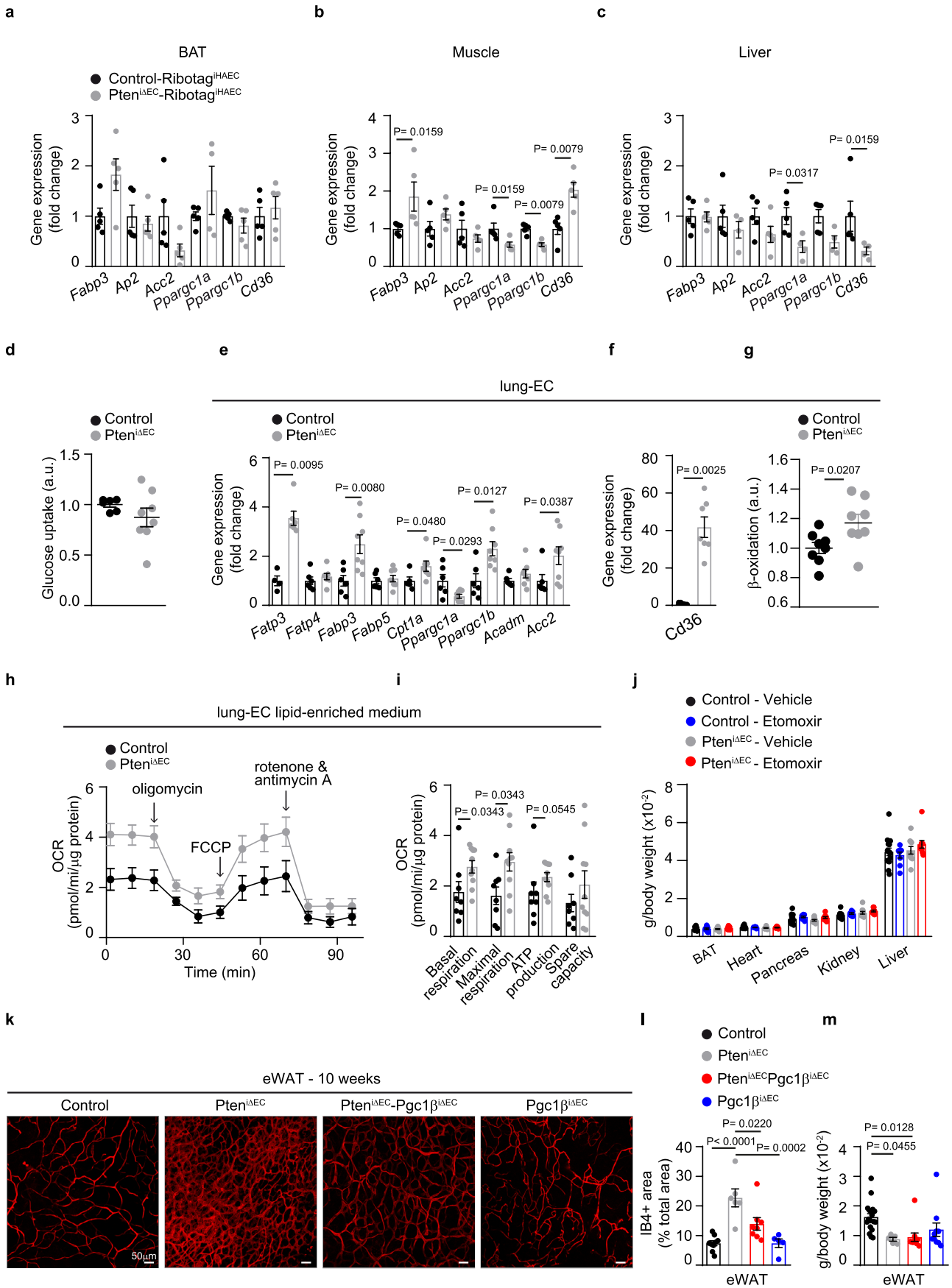

Extended Data Fig. 7 | See next page for caption.

Extended Data Fig. 7 | *Pten*-null ECs proliferation depends on lipid oxidation. (**a**-**c**) Endothelial expression of lipid catabolic genes analysed by qPCR and normalized by *mL32* gene expression in (**a**) BAT (control *Ribotag*^{iHAEC} n = 5, *Pten*$^{i\Delta EC}$- *Ribotag*^{iHAEC} n = 4), (**b**) muscle (control *Ribotag*^{iHAEC} n = 5, *Pten*$^{i\Delta EC}$-*Ribotag*^{iHAEC} n = 5), (**c**) and liver (control *Ribotag*^{iHAEC} n = 5, *Pten*$^{i\Delta EC}$ n = 4) from control *Ribotag*^{iHAEC} and *Pten*$^{i\Delta EC}$- *Ribotag*^{iHAEC} mice at 5 weeks of age. (**d**) Glucose uptake measurement in control and *Pten*$^{i\Delta EC}$ endothelial cells (control n = 6, *Pten*$^{i\Delta EC}$ n = 8). (**e** and **f**) *In vitro* expression analysis of (**e**) lipid catabolic genes and (**f**) *Cd36* by qPCR in control and *Pten*$^{i\Delta EC}$ lung-derived primary endothelial cells (lung-EC) (control n = 4, *Pten*$^{i\Delta EC}$ n = 6). (**g**) Fatty Acid β-Oxidation (FAO) in lung-EC from control and *Pten*$^{i\Delta EC}$ mice (n = 8 per group). (**h**) OCR in control and *Pten*$^{i\Delta EC}$ lung-EC in lipid-enriched medium. (**i**) Bars show OCR quantification from control and *Pten*$^{i\Delta EC}$ lung-EC in lipid-enriched medium (control n = 8, *Pten*$^{i\Delta EC}$ n = 10). (**j**) Tissue weight in control and *Pten*$^{i\Delta EC}$ mice treated with vehicle or etomoxir for 5 weeks (control - vehicle n = 15, control - etomoxir n = 9, *Pten*$^{i\Delta EC}$ - vehicle n = 11, *Pten*$^{i\Delta EC}$ - etomoxir n = 10). (**k**) Representative images of IB4 stained blood vessels (red) in flat-mounted eWAT from control, *Pten*$^{i\Delta EC}$, *Pten*$^{i\Delta EC}$-*Pgc1β*$^{i\Delta EC}$ and *Pgc1β*$^{i\Delta EC}$ mice at 10 weeks of age. (**l**) Quantification of IB4 positive area in eWAT from control, *Pten*$^{i\Delta EC}$, *Pten*$^{i\Delta EC}$-*Pgc1β*$^{i\Delta EC}$ and *Pgc1β*$^{i\Delta EC}$ mice at 10 weeks of age (control n = 9, *Pten*$^{i\Delta EC}$ n = 6, *Pten*$^{i\Delta EC}$-Pgc1β$^{i\Delta EC}$ n = 8, Pgc1β$^{i\Delta EC}$ n = 5). (**m**) eWAT pad weight of control *Pten*$^{i\Delta EC}$, *Pten*$^{i\Delta EC}$-*Pgc1β*$^{i\Delta EC}$ and *Pgc1β*$^{i\Delta EC}$ mice at 10 weeks of age (control n = 18, *Pten*$^{i\Delta EC}$ n = 5, *Pten*$^{i\Delta EC}$ - *Pgc1β*$^{i\Delta EC}$ n = 10, *Pgc1β*$^{i\Delta EC}$ n = 10). Data represent mean ± SEM (error bars). Samples represent biological replicates. All statistical analysis was performed by the two-sided Mann-Whitney test (Extended Data Fig. 7a, b, c, d, e, f, e, i, j) and one-way ANOVA with Bonferroni correction (Extended Data Fig. 7l, m).

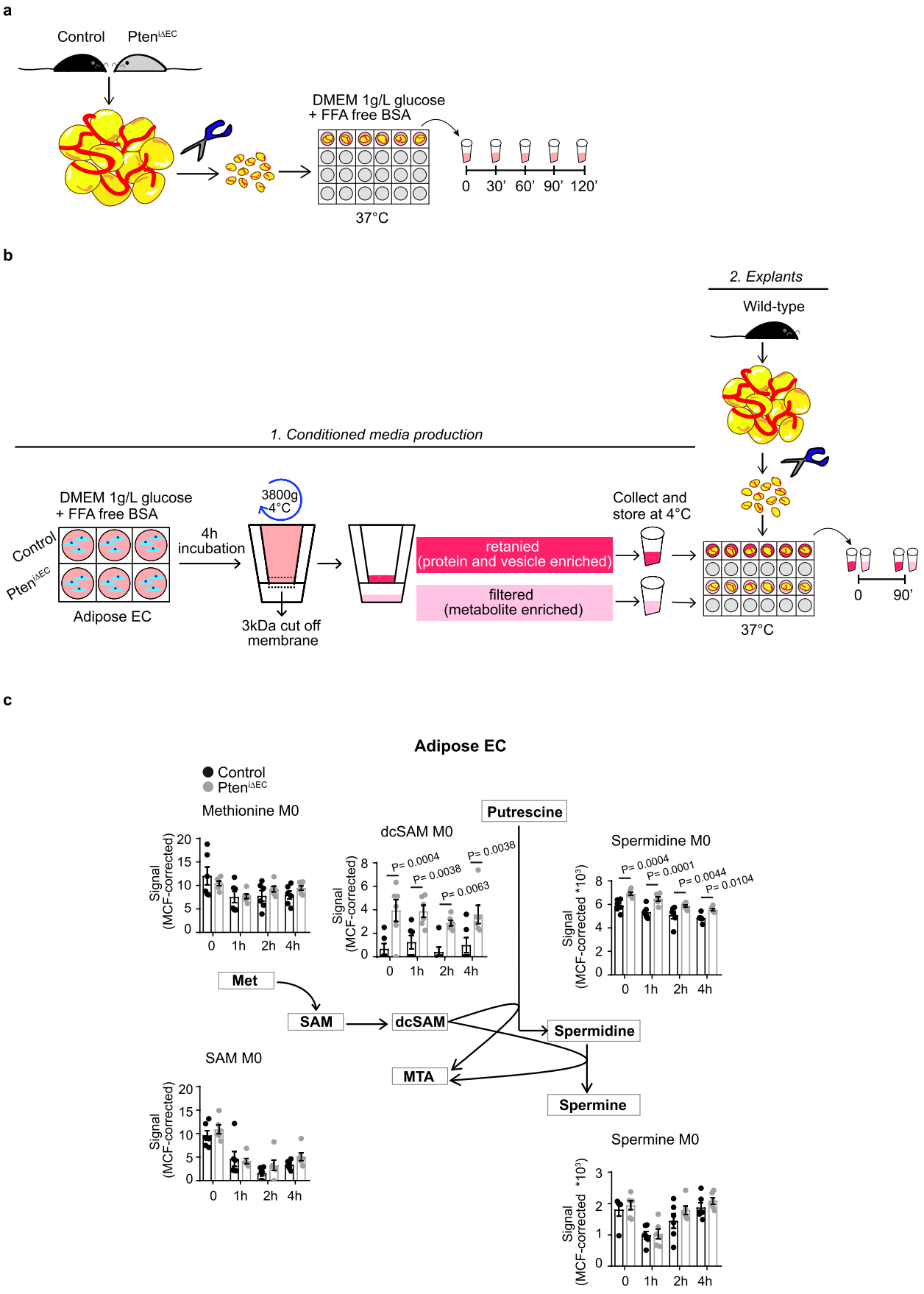

Extended Data Fig. 8 | See next page for caption.

Extended Data Fig. 8 | Loss of endothelial *Pten* results in increased polyamine levels. (**a**) Schematic representation of control and *Pten*$^{i\Delta EC}$ eWAT explant experiment. eWAT from 5 weeks of age control and *Pten*$^{i\Delta EC}$ mice were cut in ~25 mg pieces, placed in 500ul of DMEM low glucose + 0,5% FFA free BSA, and incubated for the indicated time points. (**b**) Experimental design of conditioned media collection and fractioning. A 3 kDa cut off filter retained the protein and vesicle fraction, whereas the metabolite-rich fraction was collected as the flow-through. The lipolytic effect of both fractions was tested on eWAT explants of wild-type mice. (**c**) Label-free ^{13}C fraction of metabolites related to polyamines biosynthesis in adipose-ECs from control and *Pten*$^{i\Delta EC}$ mice (n = 6 per group) from Fig. 6g. MET: Methionine; SAM: S-Adenosylmethionine; dcSAM: Decarboxylated S-adenosylmethionine; MTA: 5´ Methylthioadenosine. Data represent mean ± SEM (error bars). Statistical analysis was performed by t-test (Extended Data Fig. 8c).

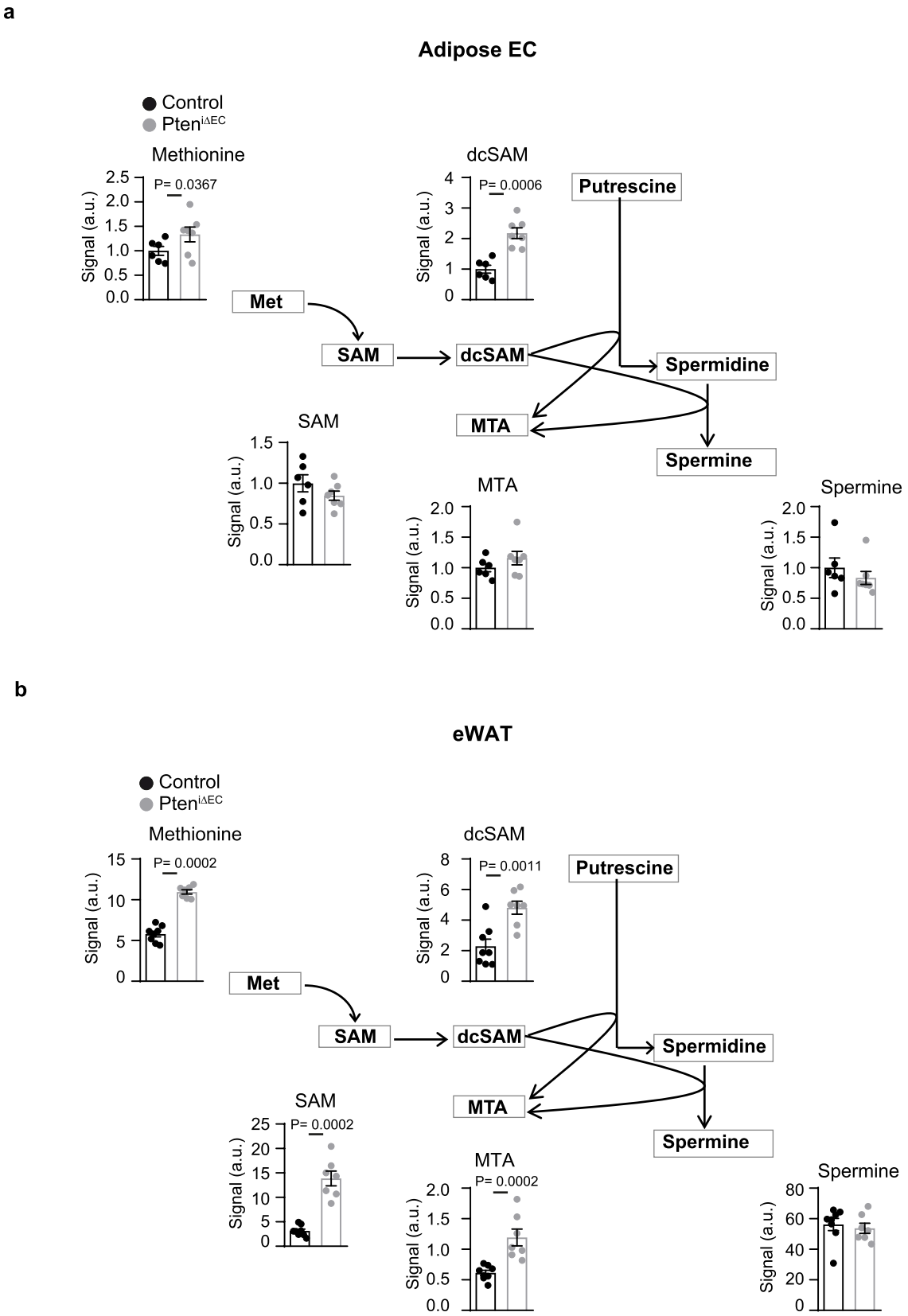

Extended Data Fig. 9 | Loss of endothelial *Pten* results in increased label-free polyamine levels. (**a**, **b**) Schematic representation of the polyamine metabolic pathway and expression of the indicated metabolites in (**d**) adipose endothelial cells (control n = 6, $Pten^{i\Delta EC}$ n = 6) and (**e**) eWAT (control n = 8, $Pten^{i\Delta EC}$ n = 7) measured by LCMS. Data represent mean ± SEM (error bars). Statistical analysis was performed by t-test (Extended Data Fig. 9a,b).

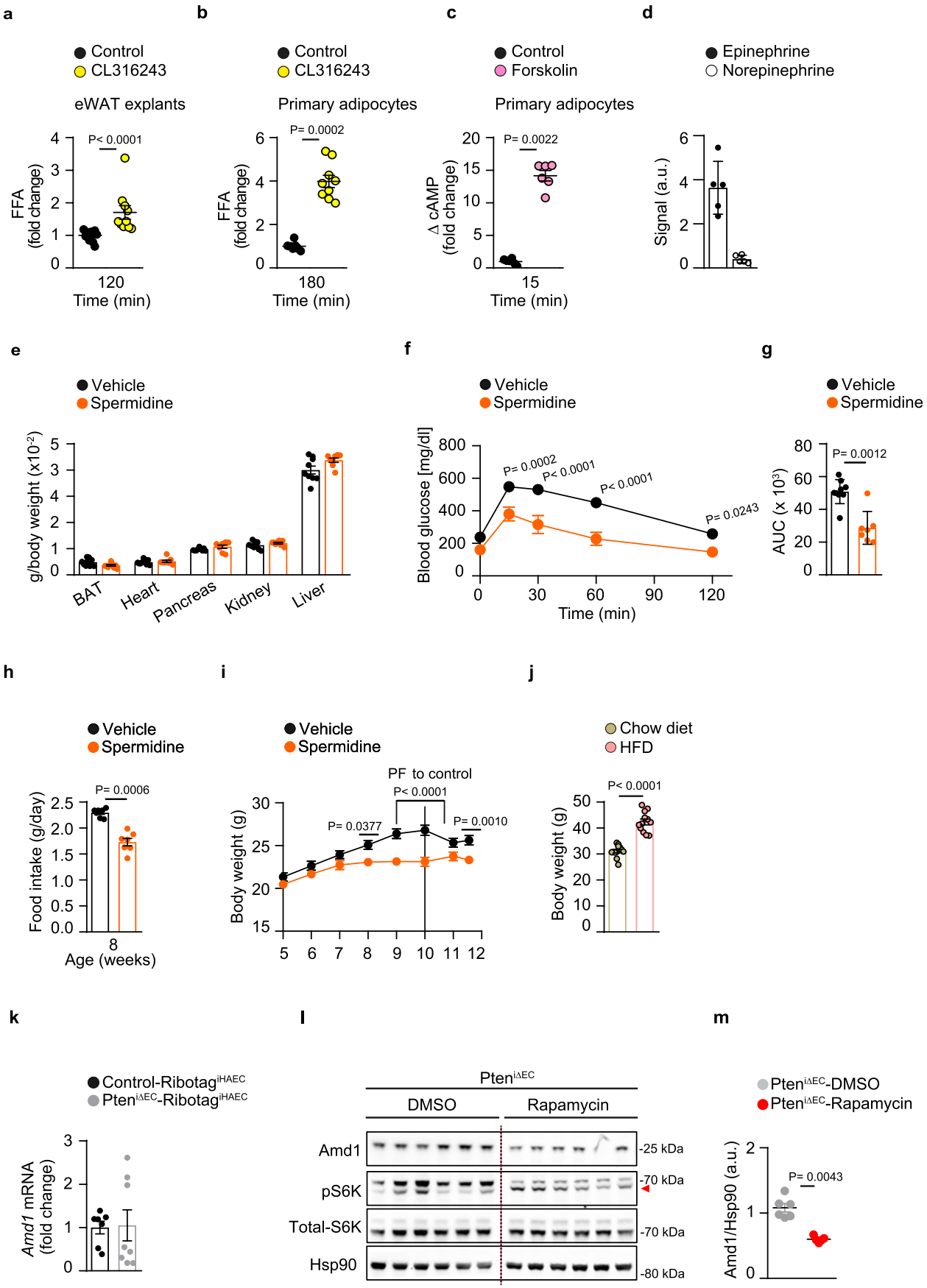

Extended Data Fig. 10 | See next page for caption.

Extended Data Fig. 10 | Spermidine supplementation in mice exposed to HFD ameliorates glucose systemic metabolism. (a, b) Positive control of lipolysis in (a) WAT tissue explants and (b) primary adipocytes. (c) Positive control of cAMP production in primary adipocytes. (d) Epinephrine and norepinephrine level in control eWAT measured by LCMS (n = 5). Data represent mean ± SEM (error bars). (e) Tissue weight of wild-type mice fed with HFD and treated with vehicle or spermidine for 6 weeks (vehicle n = 9, spermidine n = 10). (f) GTT performed in wild-type fed with HFD and treated with vehicle or spermidine for 6 weeks (vehicle n = 9, spermidine n = 7). (g) AUC quantification of blood glucose monitoring during GTT. (h) Food intake measurement in wild-type mice fed with HFD and treated with vehicle or spermidine for 6 weeks (n = 7). (i) Body weight curve of wild-type mice fed with HFD and treated with vehicle or spermidine with pair-feeding conditions after week 10. PF, Pair feeding applied to control mice (n = 7). (j) Body weight at sacrifice values of chow and HFD wild-type mice used for experiments represented in Fig. 7k (n = 12 per group). (k) *Amd1* mRNA expression levels analysed by qPCR normalized by *mL32* gene expression in eWAT endothelium from control *Ribotag*^{iHAEC} and *Pten*$^{i\Delta EC}$- *Ribotag*^{iHAEC} (control *Ribotag*^{iHAEC} n = 7, *Pten*$^{i\Delta EC}$- *Ribotag*^{iHAEC} n = 8). (l) Western blot analysis of Amd1, S6K (phosphorylated and total) in adipose-derived primary endothelial cells from *Pten*$^{i\Delta EC}$ mice after treatment with vehicle (DMSO) or mTOR inhibitor (rapamycin, 1 µm) (n = 6). Red arrowhead shows residual phosphorylated Akt signal. (c) Quantification of Amd1 signal obtained in immunoblots showed in (m) (vehicle n = 6, rapamycin n = 5). Data represent mean ± SEM (error bars). Samples represent biological replicates. Statistical analysis was performed by the two-sided Mann-Whitney test (Extended Data Fig. 10a, b, c, e, g, h, j, m) and ANOVA with Bonferroni correction (Extended Data Fig. 10f, i).

nature portfolio

Corresponding author(s): Mariona Graupera

Last updated by author(s): 24/01/2022

Reporting Summary

Nature Portfolio wishes to improve the reproducibility of the work that we publish. This form provides structure for consistency and transparency in reporting. For further information on Nature Portfolio policies, see our Editorial Policies and the Editorial Policy Checklist.

Statistics

For all statistical analyses, confirm that the following items are present in the figure legend, table legend, main text, or Methods section.

n/a	Confirmed	
☐	☒	The exact sample size (*n*) for each experimental group/condition, given as a discrete number and unit of measurement
☐	☒	A statement on whether measurements were taken from distinct samples or whether the same sample was measured repeatedly
☐	☒	The statistical test(s) used AND whether they are one- or two-sided *Only common tests should be described solely by name; describe more complex techniques in the Methods section.*
☒	☐	A description of all covariates tested
☒	☐	A description of any assumptions or corrections, such as tests of normality and adjustment for multiple comparisons
☐	☒	A full description of the statistical parameters including central tendency (e.g. means) or other basic estimates (e.g. regression coefficient) AND variation (e.g. standard deviation) or associated estimates of uncertainty (e.g. confidence intervals)
☐	☒	For null hypothesis testing, the test statistic (e.g. *F*, *t*, *r*) with confidence intervals, effect sizes, degrees of freedom and *P* value noted *Give P values as exact values whenever suitable.*
☒	☐	For Bayesian analysis, information on the choice of priors and Markov chain Monte Carlo settings
☒	☐	For hierarchical and complex designs, identification of the appropriate level for tests and full reporting of outcomes
☒	☐	Estimates of effect sizes (e.g. Cohen's *d*, Pearson's *r*), indicating how they were calculated

Our web collection on statistics for biologists contains articles on many of the points above.

Software and code

Policy information about availability of computer code

Data collection	Image acquisition was done with Leica Application Suite 2.7.3.9723 and NIS-Elements Elementary 3.2. Data on mitochondrial respiration were acquired using DatLab version 7.1.0.39 de Oroboros Instruments. Seahorse Wave Controller 2.4.1 Software was used to acquire Seahorse measurements. Locomotor activity was registered using TSE LabMaster software (TSE Systems, version 2009). Flir Tools software (version 2012) was used for thermographic recordings. Metabolomic data was acquired using QuanLynx software 4.2 from Waters.
Data analysis	Images were processed using Volocity Demo 6.0.1 and Adobe Photoshop CS5 12.0.4 and quantified with ImageJ v1.44o. Adipocytes area was calculated with the Adiposoft tool 1.14 of ImageJ software. Data on mitochondrial respiration were analyzed using DatLab version 7.1.0.39 de Oroboros Instruments. Seahorse Wave Desktop 2.6.0 Software was used to analyse Seahorse measurements. Locomotor activity was analysed using TSE LabMaster software (TSE Systems, version 2009). Flir Tools software (version 2012) was used for the analysis of thermographic images. Metabolomic data was analysed using QuanLynx software 4.2 from Waters. Data was analysed using GraphPad Prism 8.0.1(Graphpad Software Inc.).

For manuscripts utilizing custom algorithms or software that are central to the research but not yet described in published literature, software must be made available to editors and reviewers. We strongly encourage code deposition in a community repository (e.g. GitHub). See the Nature Portfolio guidelines for submitting code & software for further information.

Data

Policy information about availability of data

All manuscripts must include a data availability statement. This statement should provide the following information, where applicable:

- Accession codes, unique identifiers, or web links for publicly available datasets
- A description of any restrictions on data availability
- For clinical datasets or third party data, please ensure that the statement adheres to our policy

Image source data and Excel files of all data presented in graphs within the Figures and Extended Data have been supplied in Source Data files. Separate files for each figure has been supplied. Refer to inventory of supporting information for details.

Field-specific reporting

Please select the one below that is the best fit for your research. If you are not sure, read the appropriate sections before making your selection.

☒ Life sciences ☐ Behavioural & social sciences ☐ Ecological, evolutionary & environmental sciences

For a reference copy of the document with all sections, see nature.com/documents/nr-reporting-summary-flat.pdf

Life sciences study design

All studies must disclose on these points even when the disclosure is negative.

Sample size	No statistical methods were used to predetermine sample size. We have aimed to have experimental groups of 7-15 mice for in vivo experiments. This group sampling was based on our expertise (minimum number of mice to provide robust and reliable data) and was feasible to obtain within our animal resources. For in vitro and ex vivo studies, 4-6 biological replicates (cells or explants obtained from different mice). As with in vivo experiments, this calculation is based on our expertise.
Data exclusions	No data was excluded from the analysis. Those mice showing distress features not compatible with our ethic protocols were sacrified.
Replication	Experimental technical duplicates were included in all measurements in this study, ensuring the reproducibility of the data. In vivo data are pools of independent experimental groups, as well as in vitro data, that come for at least 3 independent experiments.
Randomization	For in vivo experiments, mice were weighted at time 0 and homogenously distributed in experimental groups. All other criteria were not considered and as such, randomized. For in vitro and ex vivo studies, samples were randomized.
Blinding	Mice and samples received a correlative number independent of their genotype, ensuring the blindness of data collection and analysis.

Reporting for specific materials, systems and methods

We require information from authors about some types of materials, experimental systems and methods used in many studies. Here, indicate whether each material, system or method listed is relevant to your study. If you are not sure if a list item applies to your research, read the appropriate section before selecting a response.

Materials & experimental systems

n/a	Involved in the study
☐	☒ Antibodies
☒	☐ Eukaryotic cell lines
☒	☐ Palaeontology and archaeology
☐	☒ Animals and other organisms
☐	☒ Human research participants
☒	☐ Clinical data
☒	☐ Dual use research of concern

Methods

n/a	Involved in the study
☒	☐ ChIP-seq
☒	☐ Flow cytometry
☒	☐ MRI-based neuroimaging

Antibodies

Antibodies used	In our study antibodies were used for immunofluorescence, immunoprecipitation and Western blot. All the antibodies described below have been extensively used by ourselves and others and validated by the manufacturer. Specific use of all antibodies is detailed below: 1. Isolectin GS-B4 568, dilution 1:200, Invitrogen cat I21412, lot 2041650

2. Isolectin GS-B4 647, dilution 1:200, Invitrogen cat I32450, lot 1977340

3. Erg, dilution 1:200, Abcam cat ab92513, lot GR3220764-3

4. Ki-67, dilution 1:200, Thermo Fisher Scientific cat 14-5698-82, lot 2002315

5. Cleaved-caspase 3, dilution 1:50, Cell Signaling Technology cat 9664S, lot 01/2015 20

6. ICAM2 (CD102), dilution 1:100, BD Pharmingen cat 553326, lot 9298692

7. HA, dilution 1:100, Sigma-Aldrich cat H6908, lot 115M48472V

8. CD31, dilution 1:100, BD Pharmingen cat A11077, lot 4338550

9. UCP1, dilution 1:1000, Abcam cat ab10983, lot GR197362-1

10. VE-cadherin, dilution 1:500, Santa Cruz cat sc-6458, lot L21121

11. p-Akt Ser473, dilution 1:1000, Cell Signaling Technology cat 4060S, lot 05/2017 23

12. Akt, dilution 1:1000, Cell Signaling Technology cat 9272S, lot 09/2014 25

13. PTEN, dilution 1:1000, Cell Signaling Technology cat 9559, lot 05/2015 12

14. p-ERK, dilution 1:1000, Cell Signaling Technology cat 9102, lot 08/2011 23

15. ERK, dilution 1:1000, Cell Signaling Technology cat 9101, lot 02/2017 30

16. B-actin, dilution 1:50000, Abcam cat ab49900, lot GR37159-1

17. HA, dilution 1:50000, Covance cat MMS-101R, lot B274467

18. AMD1, dilution 1:500, Proteintech cat 11052-1-AP, lot 00001692

19. Hsp90, dilution 1:1000, Cell Signaling Technology cat 4874, lot 2019 4

20. Anti-rat Alexa Fluor 488, dilution 1:200, Invitrogen cat A11006, lot 1689880

21. Anti-rabbit Alexa Fluor 568, dilution 1:200, Invitrogen cat A11011, lot 1942295

22. Anti-rabbit Alexa Fluor 647, dilution 1:200, Invitrogen cat A31573, lot 1693297

23. Anti-rabbit HRP, dilution 1:5000, DAKO cat P0399, lot 20043737

24. Anti-mouse HRP, dilution 1:5000, DAKO cat P0260, lot 20022144

25. Anti-goat HRP, dilution 1:5000, DAKO cat P0449, lot 20071317

The information above can also be found in Supplementary Table 4. Some of these antibodies are heavily used in the lab and different lot numbers may have been used during the development of the project. However, we have seen no variation between lot numbers in more than 5 years of use.

Validation

Antibodies 1,2,10,11,13 were previously validated in our article Serra et al. Nat Commun. 2015 Jul 31;6:7935. doi: 10.1038/ncomms8935

Antibody 8 was previously validated in our article Soler et al. Clin Cancer Res. 2016 Dec 1;22(23):5805-5817. doi: 10.1158/1078-0432.CCR-15-3051.

Antibodies 3,6,12, 16,20-25 were previously validated in our article Angulo-Urarte et al. Nat Commun. 2018 Nov 16;9(1):4826. doi: 10.1038/s41467-018-07172-3.

Antibodies 14 & 15 were previously validated in our article Figueiredo et al. Circulation. 2020 Aug 18;142(7):688-704. doi: 10.1161/CIRCULATIONAHA.119.042354

Antibody 18 was previously validated in our article Zabala-Letona et al. Nature. 2017 Jul 6;547(7661):109-113. doi: 10.1038/nature22964.

Antibody 19 was previously validated in our article Hermanova et al. J Exp Med. 2020 Jun 1;217(6):e20191787. doi: 10.1084/jem.20191787.

Validation statement for antibody 4 can be found at https://www.thermofisher.com/antibody/product/Ki-67-Antibody-clone-SolA15-Monoclonal/14-5698-82

Validation statement for antibody 5 can be found at https://www.cellsignal.com/products/primary-antibodies/cleaved-caspase-3-

asp175-5a1e-rabbit-mab/9664

Validation statement for antibody 7 can be found at https://www.sigmaaldrich.com/ES/en/product/sigma/h6908

Validation statement for antibody 9 can be found at https://www.abcam.com/ucp1-antibody-ab10983.html

IP using antibody 17 has been validated in Extended Data Figure 1a. Only the specific transcript for endothelial cells (Cdh5) was enriched in the tissues analysed. Only these cells are expressing the HA tag in their ribosomes. Additional validation for this IP can found in the following article: Sanz et al. Proc Natl Acad Sci U S A. 2009 Aug 18;106(33):13939-44. doi: 10.1073/pnas.0907143106.

Animals and other organisms

Policy information about studies involving animals; ARRIVE guidelines recommended for reporting animal research

Laboratory animals	Mice were under controlled housing conditions of temperature (20-24ºC), humidity (45-65%) and dark/light exposure (10h/14h). The following mouse strains were used: C57Bl6 mice (purchased from Charles River), PdgfbiCreERT2; PTENflox/flox, PdgfbiCreERT2;Ribotagflox/flox, PdgfbiCreERT2;PTENflox/flox;Ribotagflox/flox, PdgfbiCreERT2; PTENflox/flox; PGC1b flox/flox, PdgfbiCreERT2; PGC1b flox/flox, Cdh5iCreERT2; PTENflox/flox mice and control littermates (cre negative). All animals were backcrossed on a C57BL6/J genetic background. Adult male mice were used for all experiments with ages ranging 4- and 34 weeks. Adult female mice were used as source of primary endothelial cells.
Wild animals	No wild animals were used in the study.
Field-collected samples	No field-collected samples were used in the study.
Ethics oversight	Experiments were conducted in accordance with the guidelines and laws of the Catalan Departament d'Agricultura, Ramaderia i Pesca (Catalunya, Spain), following protocols approved by the local Ethics Committees of IDIBELL-CEEA.

Note that full information on the approval of the study protocol must also be provided in the manuscript.

Human research participants

Policy information about studies involving human research participants

Population characteristics	We studied omental WAT from morbid obese patients (BMI>35) and non-obese patients (BMI<30). For the study of polyamine levels, 12 obese female patients (BMI of 42.9±4.9) and 6 non-obese females (BMI of 26.7±1.5) age-matched (≥ 53) were included. For vascular analysis and Pten mRNA expression analysis, ≥ 6 morbidy obese (BMI of 42.84±4,43, 3 females and 7 males, age of 52±13,24 years) and 6 non-obese individuals (BMI of 26.86±2.8, 1 female and 5 males, age of 60.5±5.31 years) were included.
Recruitment	We studied omental WAT from morbid obese patients (BMI>35) undergoing bariatric surgery and non-obese patients (BMI<30) subjects undergoing abdominal surgery at the Hospital Clinic de Barcelona. No self-selection bias is predicted, as BMI was the only parameter considered for recruitment.
Ethics oversight	The Hospital Clinic of Barcelona Ethical Committee approved the studies, and all study participants provided informed consent to donate tissue samples.

Note that full information on the approval of the study protocol must also be provided in the manuscript.